AGU PUBLICATIONS

Tectonics

RESEARCH ARTICLE
10.1002/2013TC003501

Key Points:
- Three periods of granitoids intrusion and tectonic settings are determined
- A long-lived accretionary orogenic model is proposed for southwest CAOB
- The model links the early history of the CAOB with Rodinia evolution

Supporting Information:
- Readme
- Table S1
- Table S2
- Table S3
- Text S1

Correspondence to:
W. Zhu,
zwb@nju.edu.cn

Citation:
Ge, R., W. Zhu, S. A. Wilde, J. He, X. Cui, X. Wang, and Z. Bihai (2014), Neoproterozoic to Paleozoic long-lived accretionary orogeny in the northern Tarim Craton, *Tectonics*, *33*, 302–329, doi:10.1002/2013TC003501.

Received 9 DEC 2013
Accepted 15 FEB 2014
Accepted article online 24 FEB 2014
Published online 26 MAR 2014

Neoproterozoic to Paleozoic long-lived accretionary orogeny in the northern Tarim Craton

Rongfeng Ge[1,2], Wenbin Zhu[1], Simon A. Wilde[2], Jingwen He[1], Xiang Cui[1], Xi Wang[1], and Zheng Bihai[1]

[1]State Key Laboratory for Mineral Deposits Research, School of Earth Science and Engineering, Nanjing University, Nanjing, China, [2]Department of Applied Geology, Curtin University, Perth, Western Australia, Australia

Abstract The Tarim Craton, located in the center of Asia, was involved in the assembly and breakup of the Rodinia supercontinent during the Neoproterozoic and the subduction-accretion of the Central Asian Orogenic Belt (CAOB) during the Paleozoic. However, its tectonic evolution during these events is controversial, and a link between the Neoproterozoic and Paleozoic tectonic processes is missing. Here we present zircon U-Pb ages, Hf isotopes, and whole-rock geochemical data for the extensive granitoids in the western Kuruktag area, northeastern Tarim Craton. Three distinct periods of granitoid magmatism are evident: circa 830–820 Ma, 660–630 Ma, and 420–400 Ma. The magma sources, melting conditions (pressure, temperature, and water availability), and tectonic settings of various granitoids from each period are determined. Based on our results and the geological, geochronological, geochemical, and isotopic data from adjacent areas, a long-lived accretionary orogenic model is proposed. This model involves an early phase (circa 950–780 Ma) of southward advancing accretion from the Tianshan to northern Tarim and a late phase (circa 780–600 Ma) of northward retreating accretion, followed by back-arc opening and subsequent bidirectional subduction (circa 460–400 Ma) of a composite back-arc basin (i.e., the South Tianshan Ocean). Our model highlights a long-lived accretionary history of the southwestern CAOB, which may have initiated as part of the circum-Rodinia subduction zone and was comparable with events occurring at the southern margin of the Siberian Craton, thus challenging the traditional southward migrating accretionary models for the CAOB.

1. Introduction

Accretionary orogens occur at intraoceanic and continental convergent plate boundaries due to subduction of oceanic plate. They are made up of accretionary wedges, magmatic arcs, and back-arc domains and often incorporate various microcontinents, oceanic plateaus, seamounts, and ophiolite mélanges in the accretionary wedges. According to their geological characteristics, accretionary orogens can be subdivided into advancing type and retreating type, as characterized by the modern Andes and West Pacific, respectively [*Cawood et al*., 2009]. One important difference between advancing and retreating subduction-accretion lies in the back-arc region, where the former is dominated by significant crustal thickening, anatexis, and development of retroarc foreland basins, whereas the latter is characterized by crustal thinning and back rifting [*Cawood et al*., 2009]. Tectonic switching between these two types of accretionary orogen has been widely documented in the geological history and has been commonly attributed to a change in dynamic style [e.g., *Uyeda and Kanamori*, 1979; *Collins*, 2002a, 2002b; *Schellart*, 2008; *Lister and Forster*, 2009; *Cawood et al*., 2009].

In terms of the evolution of a supercontinent, two fundamentally different types of accretionary orogens have been recognized: interior and exterior (periphery) [*Murphy and Nance*, 1991; *Collins et al*., 2011]. Interior accretionary orogens (e.g., the Brasiliano and Kuunga orogens) occur between converging continental blocks and are followed by continent-continent collision, leading to the assembly of a supercontinent. In contrast, exterior accretionary orogens (e.g., the Terra Australis Orogen) usually initiate at the periphery of a supercontinent following its final assemblage, in order to balance the ongoing sea floor spreading in the circum-supercontinent ocean [*Murphy and Nance*, 1991; *Cawood*, 2005; *Cawood and Buchan*, 2007]. *Li and Zhong* [2009] proposed that it is the circum-supercontinent subduction that leads to the rise of a superplume as a result of mantle avalanche, which finally results in the breakup of a supercontinent. Therefore, distinguishing interior and exterior accretionary orogens is crucial for understanding the reconstruction and evolution of supercontinents.

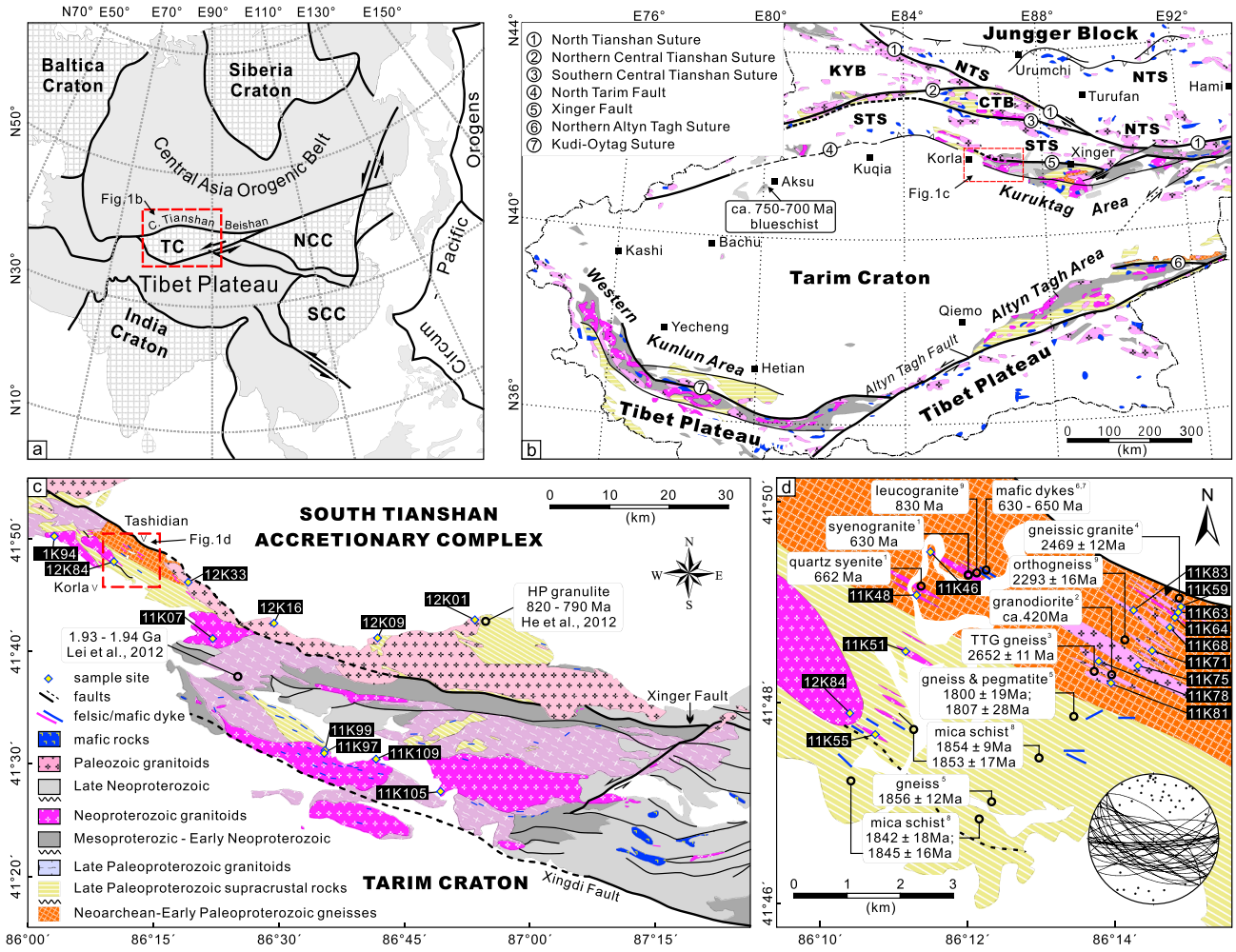

Figure 1. (a) Simplified tectonic map of Eurasia showing the major tectonic units and the location of the TC: Tarim Craton, NCC: North China Craton, and SCC: South China Craton. Note the position of Chinese (C.) Tianshan and Beishan orogens. (b) Simplified geological map of the Tarim Craton [after *XBGMR*, 1993], showing the main tectonic subdivisions, Precambrian (meta)sedimentary rocks, and granitoid and mafic rocks. CTB: Central Tianshan Block; KYB: Kazakhstan-Yili Block; NTS; North Tianshan accretionary complex; STS: South Tianshan accretionary complex. Note the locations of the Kuruktag area and the circa 750–700 Ma Aksu blueschist. Legend is in Figure 3c. (c) Simplified geological map of the western Kuruktag area [after *XBGMR*, 1993]. Note the occurrence of the Paleozoic granitoid belt to the north of the Neoproterozoic one. The circa 820–790 Ma granulites and circa 1.93–1.94 Ga granitoids reported by *He et al.* [2012] and *Lei et al.* [2012], respectively, are also shown. (d) Simplified geological map of the Korla area [after *XBGMR*, 1993]. The insert shows the stereographic projection of the main foliation. Geochronological data are cited from 1 - *Ge et al.* [2012a]; 2 - *Ge et al.* [2012b]; 3 - *Long et al.* [2011b]; 4 - *Shu et al.* [2011]; 5 - *Zhang et al.* [2012b]; 6 - *Zhu et al.* [2008]; 7 - *Zhu et al.* [2011a]; 8 - *Ge et al.* [2013b]; and 9 - *Ge et al.* [2013a].

The Tarim Craton, located in the center of Asia (Figure 1a), was considered as part of the Rodinia supercontinent during the Neoproterozoic [e.g., *Li et al.*, 1996, 2008, 2013]. Based on correlation of paleomagnetic poles [e.g., *Chen et al.*, 2004; *Zhan et al.*, 2007; *Wen et al.*, 2013; *Zhao et al.*, 2014], glacial diamictite-bearing sedimentary sequences [e.g., *Li et al.*, 1996; *Xu et al.*, 2009; *He et al.*, 2014] and magmatic events [e.g., *Lu et al.*, 2008; *Zhang et al.*, 2012a], a Tarim-Australia-South China connection in Rodinia has been widely recognized, although the detailed reconstruction is still controversial. Studies over the last decade have documented extensive and diverse Neoproterozoic magmatism between 830 and 615 Ma in the Tarim Craton, which has been uncritically interpreted as a result of rifting events due to multiple episodes of a superplume activity during the breakup of Rodinia [e.g., *Xu et al.*, 2005, 2009, 2013; *Zhang et al.*, 2007, 2009a, 2009b, 2012a; *Long et al.*, 2011a; *Shu et al.*, 2011]. However, direct evidence for mantle plume activity (e.g., komatiite, high-Mg basalt, oceanic island basalts (OIB), and flood basalt) is lacking in northern Tarim, although some OIB-like gabbros were found in southern Tarim [*Zhang et al.*, 2006]. The presence of circa 750–700 Ma high-pressure/low-temperature (HP/LT) blueschist [*Liou et al.*, 1989, 1996; *Nakajima et al.*, 1990; *Zhu et al.*, 2011a; *Yong et al.*, 2012] and the circa 830–790 Ma high-grade (high-pressure?)

metamorphic rocks [*He et al*., 2012; *Ge et al*., 2013a] suggests that subduction and accretion were probably operating in northern Tarim during the same period and may be an important geodynamic factor.

During the Paleozoic, the Tarim Craton was involved in the evolution of the Tianshan orogen, which occupies the southwestern part of the Central Asian Orogenic Belt (CAOB). However, the Paleozoic tectonic activity of northern Tarim is highly controversial. Based on the dominance of carbonate rocks in the Cambrian-Ordovician, most researchers suggested that the northern Tarim was a passive continental margin, which subducted northward (present coordinates) and collided with the Tianshan orogens [e.g., *Sengör et al*., 1993; *Windley et al*., 2007; *Han et al*., 2011; *Xiao et al*., 2010, 2013]. However, another group of researchers proposed an active margin model involving southward subduction beneath the Tarim Craton, detachment of the Central Tianshan arc with back-arc opening of the Southern Tianshan Ocean, and subsequent closure of the back-arc basin by southward subduction beneath the rifted Tarim margin [*Charvet et al*., 2007, 2011; *Lin et al*., 2009, 2013; *Wang et al*., 2010, 2011; *Ma et al*., 2014]. This model is mainly based on ductile deformation features of the accretionary complexes in the Chinese Tianshan. Recently, Late Ordovician-Early Devonian arc-related granitoids and volcanic rocks have been identified in the northern margin of Tarim, supporting the southward subduction model [*Ge et al*., 2012a; *Guo et al*., 2013a, 2013b; *Jia et al*., 2013; *Lin et al*., 2013; *Huang et al*., 2013a]. Detrital zircon data from the Central Tianshan also suggest a derivation from Tarim [*Ma et al*., 2011, 2012]. However, evidence for Ordovician-Silurian rifting and extension associated with the opening of the South Tianshan Ocean, as suggested by the southward subduction model, is lacking in northern Tarim. The oldest ophiolite mélanges in the South Tianshan accretionary complex (circa 520–600 Ma) [*Yang et al*., 2005; *Zhang and Guo*, 2008; *Ao et al*., 2012] suggest that rifting was initiated before the Paleozoic. This raises some intriguing questions: Did the Neoproterozoic rifting event lead to the opening of the South Tianshan Ocean and separation of the Central Tianshan Block? Was this related to subduction or a mantle plume? Is Neoproterozoic subduction connected with the Paleozoic tectonic history?

Here we report zircon U-Pb-Lu-Hf isotopic and whole-rock geochemical data for Neoproterozoic and Paleozoic granitoids in the western Kuruktag area, northeastern Tarim Craton (Figure 1c). Combined with available data from adjacent regions, we propose a Neoproterozoic-Paleozoic long-lived subduction and accretion model for the northern Tarim Craton. This model links the Rodinia supercontinent with the CAOB and has implications for the early accretionary history of the CAOB.

2. Geological Setting and Samples

The Chinese Tianshan orogen, located in the southwest part of the CAOB (Figure 1a), is sandwiched between the Junggar block to the north and the Tarim Craton to the south (Figure 1b). Generally, it has been subdivided into the North Tianshan (NTS), Kazakhstan-Yili Block (KYB), Central Tianshan Block (CTB), and South Tianshan (STS) (Figure 1b). The NTS and STS are two accretionary complexes mainly composed of Paleozoic marine sedimentary rocks, ophiolite mélanges, and high- to ultrahigh-pressure (HP-UHP) metamorphic rocks, whereas the KYB and CTB are two continental arcs with Precambrian basement. These tectonic units are separated from each other by three major structural discontinuities, interpreted as sutures (Figure 1b). For detailed geology of each tectonic unit and its correlation with those in the adjacent areas, the reader is referred to recent papers by *Charvet et al*. [2011], *Gao et al*. [2011], *Han et al*. [2011], *Wilhem et al*. [2012], and *Xiao et al*. [2013].

The Tarim Craton is separated from the South Tianshan accretionary complex by the North Tarim Fault in the west, which has been interpreted as connected to the Xinger Fault [*Charvet et al*., 2011; *Han et al*., 2011] or the Xingdi Fault [*Gao et al*., 2011; *Xiao et al*., 2013] in the Kuruktag area in the east (Figure 1c). We suggest that the Xinger Fault is the tectonic boundary between Tarim and the South Tianshan, because Neoarchean-Paleoproterozoic metamorphic rocks that are considered a major part of the basement of Tarim are limited to the south of this fault (Figure 1c).

The Kuruktag (also spelled Quruqtagh or Kuluketage) area is located at the northeastern margin of the Tarim Craton and is one of the major early Precambrian basement blocks of Tarim [e.g., *Gao et al*., 1993; *Lu et al*., 2008]. The basement rocks in this area include Neoarchean TTG (tonalite-trondhjemite-granodiorite) and granitic gneisses with amphibolite and paragneiss enclaves (circa 2.65–2.51 Ga), early Paleoproterozoic orthogneiss (circa 2.47–2.46 Ga and 2.36–2.29 Ga), late Paleoproterozoic granitoids (circa 1.94–1.93 Ga), and supracrustal rocks (circa 2.0–1.85 Ga) [*Long et al*., 2010, 2011b; *Shu et al*., 2011; *Lei et al*., 2012; *Ge et al*., 2013a, 2013b]. All these rocks were metamorphosed to upper amphibolite or granulite facies at circa 1.9–1.8 Ga [*Ge et al*., 2013b,

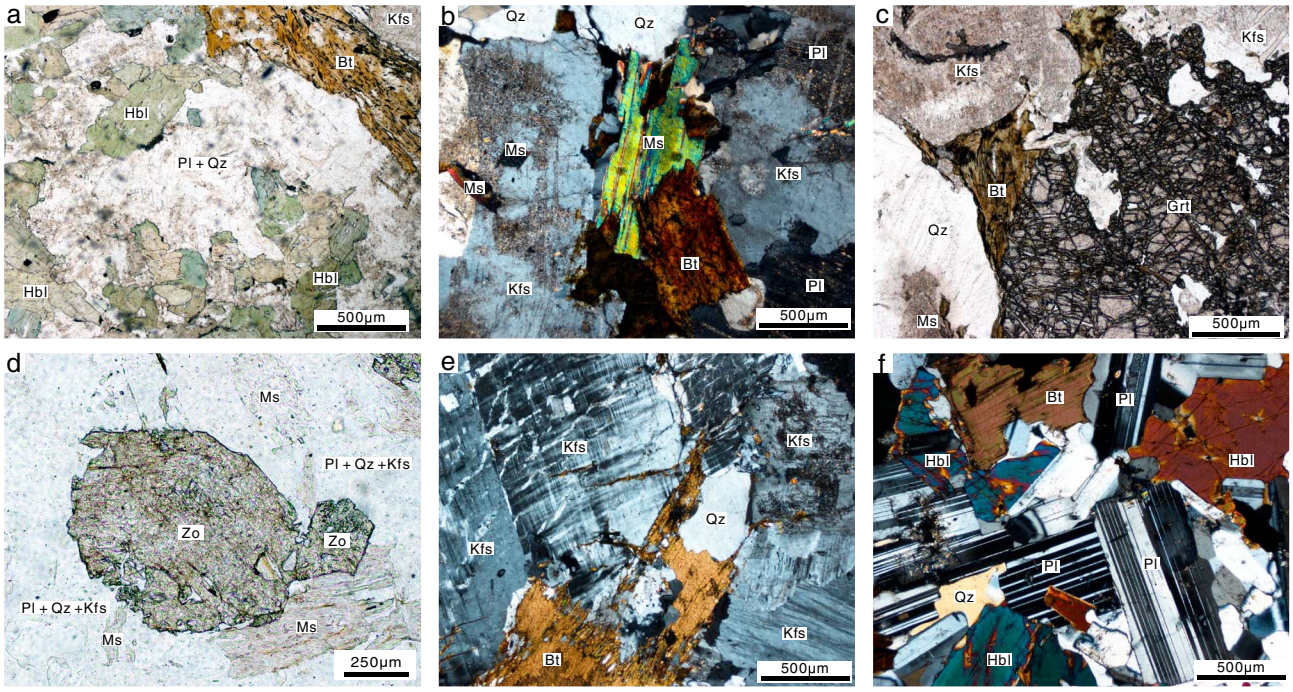

Figure 2. Photomicrographs showing typical textures and mineral assemblages of the granitoids in the western Kuruktag area. (a) Hornblende-bearing granodiorite (sample 11K97), (b) two-mica granite (sample 11K105), (c) garnet-muscovite-bearing granite (sample 11K99), (d) euhedral zoisite in garnet-muscovite-bearing granite (sample 11K94), (e) quartz syenite (sample 11K48), and (f) diorite (sample 12K09). Mineral abbreviations are as follows: Bt = biotite, Ep = epidote, Grt = garnet, Hbl = hornblende, Kfs = potassium feldspar, Ms = muscovite, Pl = plagioclase, Qz = quartz, and Zo = zoisite.

and references therein] and are unconformably overlain by Mesoproterozoic to early Neoproterozoic clastic and carbonate sedimentary rocks [*Gao et al*., 1993].

A major tectonothermal event occurred during the Neoproterozoic, resulting in extensive magmatism in the Tarim Craton. In the Kuruktag area, diverse Neoproterozoic magmatic rocks have been documented over the last decade, including (1) voluminous granitoids, mostly dated between circa 830–735 Ma and 660–630 Ma, (2) circa 800 Ma mafic-ultramafic-carbonatite complexes, (3) circa 760 Ma and 735 Ma bimodal intrusive complexes, and (4) mafic dykes swarms dated at circa 820 Ma, 780–770 Ma and 660–630 Ma (see summary in *Zhu et al*. [2011a], *Zhang et al*. [2012a], and *Ge et al*. [2012b]). It should be noted that little latest Mesoproterozoic-early Neoproterozoic magmatism has been documented in northern Tarim, except for two granitoids dated at circa 1.05 Ga and 0.93 Ga by *Shu et al*. [2011]. In contrast, circa 0.95–0.90 Ga deformed and metamorphosed magmatic rocks are abundant in the Kazakhstan-Yili and Central Tianshan blocks to the north of Tarim [*Chen et al*., 2009; *Hu et al*., 2010; *Peng et al*., 2012; *Huang et al*., 2013b].

In this study we focus on granitoid rocks in the western Kuruktag area (Figure 1c). Extensive granitoids over 2000 km^2 are exposed in this area, making up about 70% of the pre-Cenozoic outcrops. These were interpreted as Proterozoic or Paleozoic, based on geological relationships or deformation style [*Xinjiang Bureau of Geology and Mineral Resources* (*XBGMR*), 1993], but their precise intrusion ages, petrological and geochemical characteristics, and tectonic significance remain unknown. Our field observations and geochronological data indicate that they can be subdivided into four suites: late Paleoproterozoic, mid-Neoproterozoic, late Neoproterozoic, and Paleozoic. *Lei et al*. [2012] reported two LA-ICP-MS zircon ages of 1934 ± 13 Ma and 1944 ± 16 Ma for late Paleoproterozoic gneissic granitoids. The middle- and late-Neoproterozoic and Paleozoic granitoids occur as batholiths in two WNW-ESE extending magmatic belts, with the Paleozoic intrusions lying to the north (Figure 1c). Detailed cross-section measurements reveal that they also occur as 10–300 m wide dikes, stocks, or small plutons in the Korla area (Figure 1d). These granitoids are only locally deformed and intrude all the pre-Neoproterozoic rocks (Figures 1c and 1d).

Lithologically, the mid-Neoproterozoic granitoids are dominated by hornblende-bearing granodiorite (Figure 2a), two-mica (biotite and muscovite) granite (Figure 2b), with minor garnet- and muscovite-bearing granite (Figure 2c).

Table 1. Summary of Zircon U-Pb Ages and Lu-Hf Isotopic Data for the Neoproterozoic to Paleozoic Granitoids in the Western Kuruktag Area, Northern Tarim Craton

Sample No.	Lithology[a]	Zircon U-Pb Age (Ma)[b]	Initial $^{177}Hf/^{176}Hf$[d]	ε Hf (t)[d]	T_{DM}^2 (Ga)[d]	Inherited Zircon (Ga)[e]
			Mid-Neoproterozoic Granitoids			
11K07	Granodiorite (ep)	830 ± 5	0.281362–0.281631	−31.6 to −22.0	3.08–3.66	1.82–1.90, 2.07
11K97	Granodiorite (ep, hbl)	821 ± 6	0.281436–0.281805	−29.1 to −16.6	2.71–3.50	1.82–1.87, 2.20
11K94	Grt-ms granite (ep, grt, ms)	830 ± 6	0.281792–0.281936	−16.4 to −11.3	2.42–2.73	1.83–1.95, 2.16, 2.29
11K99	Grt-ms granite (grt, ms)	834 ± 6	0.281559–0.281837	−24.5 to −14.7	2.63–3.23	1.80–1.93
11K105	Two-mica granite	828 ± 7	0.281450–0.281742	−28.5 to −18.1	2.84–3.47	1.80–1.92
11K109	Two-mica granite	831 ± 6	0.281213–0.281756	−36.8 to −17.6	2.81–3.98	1.85–1.94
			Late Neoproterozoic Granitoids			
11K48	Quartz syenite (hbl)	660 ± 5	0.282228–0.282319	−4.7 to −1.5	1.68–1.88	
11K51	Quartz syenite (hbl)	659 ± 6	0.282199–0.282336	−5.7 to −0.9	1.64–1.94	
11K46	Quartz syenite (hbl)	627 ± 4	0.282243–0.282352	−4.9 to −1.1	1.63–1.87	
11K55	Syenogranite	636 ± 5	0.282239–0.282322	−4.8 to −1.9	1.69–1.87	
11K64	Syenogranite	657 ± 6	0.282255–0.282491	−3.8 to +4.5	1.30–1.82	1.80–1.94[e] (?)
12K84	Syenogranite (hbl)	653 ± 14[c]	0.282141–0.282330	−7.9 to −1.2	1.66–2.08	1.92[e]
			Paleozoic Granitoids			
11K59	Granodiorite (hbl)	418 ± 4	0.282297–0.282424	−7.6 to −3.1	1.60–1.88	
11K71	Granodiorite (hbl)	421 ± 4	0.282155–0.282438	−12.6 to −2.6	1.57–2.19	0.81–0.82, 1.71[e]
11K75	Granodiorite (hbl)	420 ± 4	0.282254–0.282420	−9.1 to −3.2	1.61–1.97	2.23, 1.91
11K78	Granodiorite (hbl)	420 ± 4	0.282099–0.282542	−14.6 to +1.1	1.33–2.31	2.89[e], 2.70, 2.50, 2.30, 2.20, 1.98–1.81, 0.82–0.83
11K81	Granodiorite (hbl)	418 ± 4	0.282285–0.282468	−8.0 to −1.5	1.50–1.91	1.76–1.81
11K63	Monzoranite (hbl)	420 ± 4	0.282351–0.282522	−5.6 to +0.4	1.38–1.77	2.26, 2.34, 1.83[e]
11K68	Monzoranite	417 ± 4	0.282382–0.282487	−4.6 to −0.9	1.46–1.69	2.67, 1.48[e], 0.95[e]
11K83	Monzoranite	420 ± 3	0.282327–0.282735	−6.5 to +8.0	0.90–1.81	2.57[e]
12K01	Monzoranite (hbl)	408 ± 5	0.282410–0.282566	−4.0 to +1.7	1.29–1.64	
12K16	Monzoranite	406 ± 4	0.281809–0.282055	−23.4 to −16.5	2.42–2.85	1.78–1.87, 0.72–0.87
12K09	Diorite	417 ± 5	0.282414–0.282583	−3.4 to +2.5	1.24–1.62	
12K33	Diorite	422 ± 4	0.282180–0.282482	−11.7 to −2.9	1.60–2.15	0.81

[a]Within brackets are characteristic minerals, ep = epidote; grt = garnet; hbl = hornblende, ms = muscovite.
[b]Weighted mean $^{206}Pb/^{238}U$ ages; errors are at 2σ.
[c]Denotes upper intercept age. See Figures 3–5 and Table S1 for details.
[d]Calculated using the weighted mean $^{206}Pb/^{238}U$ ages or upper intercept ages. See Table S2 for details and Appendix A for parameters used.
[e]Denotes discordant age.

Some hornblende-bearing granodiorite and garnet-muscovite-bearing granite contain euhedral epidote and/or zoisite (up to 15%, Figure 2d), locally with allanite cores or embayed by quartz and feldspar, which may imply a magmatic origin and a minimum emplacement pressure of the pluton of about 5–6 kbar [*Schmidt and Poli*, 2004]. In contrast, the late Neoproterozoic rocks mainly include biotite- and/or hornblende-bearing quartz syenite (Figure 2e) and syenogranite. They are closely associated with circa 650–630 Ma mafic dikes and gabbroic plutons (sensitive high-resolution ion microprobe (SHRIMP) zircon ages, *Zhu et al.* [2008, 2011b], and our unpublished data). Evidence for magma mingling and mafic granular enclaves has been observed in the field. *Ge et al.* [2012b] reported several LA-ICP-MS zircon U-Pb ages of circa 660–630 Ma for the granitoids. Local metamorphic overprinting and anatexis induced by magma intrusion have also been documented [*Ge et al.*, 2012b, 2013a]. The Paleozoic granitoids are mostly hornblende-bearing granodiorite and monzogranite, with minor biotite-bearing diorite (Figure 2f) and biotite-muscovite granite. Some of the granodiorites show a porphyritic texture with euhedral K-feldspar and plagioclase phenocrysts up to 5 cm long. Irregular mafic granular enclaves and transitional contacts between the mafic (dioritic) and felsic (granitic) magmas are common in the field. Three LA-ICP-MS zircon U-Pb ages of circa 420 Ma have been reported for porphyritic granodiorite [*Ge et al.*, 2012a].

A total of 24 samples from the middle- and late- Neoproterozoic and Paleozoic granitoids were selected for zircon dating and Lu-Hf isotopic analyses (Figures 1c and 1d). These samples, as well as additional samples from the same pluton, were also analyzed for major and trace element compositions. The analytical procedures are presented in Appendix A (supporting information). The results for zircon U-Pb ages, Hf isotopes, and geochemical data are presented in Tables S1–S3 (supporting information), respectively, and summarized in Table 1. Ages cited in the text are $^{206}Pb/^{238}U$ ages for those younger than 1000 Ma and $^{207}Pb/^{206}Pb$ ages for those older than 1000 Ma. Errors of U-Pb ages are 2σ for pooled ages and 1σ for single analyses.

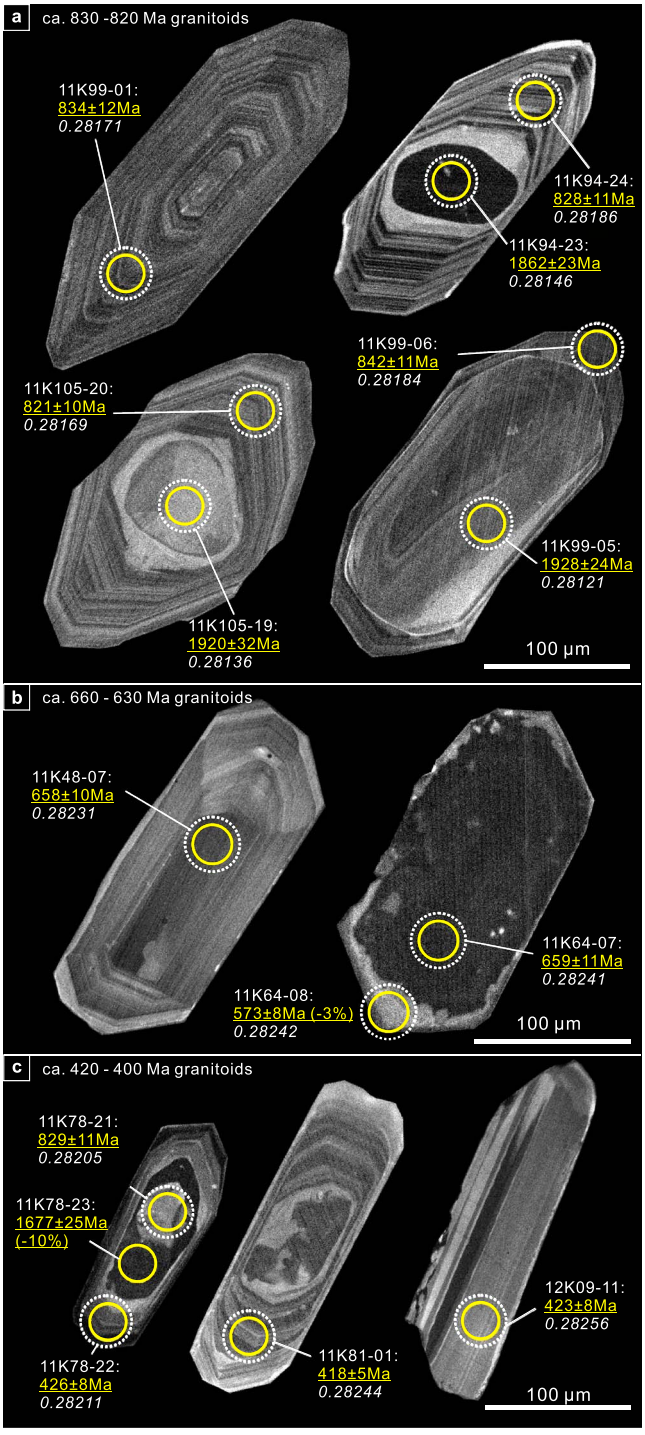

Figure 3. Representative zircon CL images for (a) the circa 830–820 Ma, (b) the circa 660–630 Ma, and (c) the circa 420–400 Ma granitoids in the Kuruktag area. The solid and dotted circles are U-Pb and Lu-Hf spots, respectively. Analytical number, apparent age (underlined), and measured $^{176}Hf/^{177}Hf$ (in italics) are denoted. The level of discordance (if any) is shown in bracket following the apparent age. Note the abundant inherited metamorphic cores in the circa 830–820 Ma zircons.

3. Results

3.1. Zircon U-Pb Ages

3.1.1. Mid-Neoproterozoic Granitoids

Samples 11K07 and 11K97 are epidote- and/or hornblende-bearing granodiorites. Zircons from these sample are colorless, transparent, and euhedral, with lengths up to 200 μm and aspect ratios of 1:2 to 1:3. Cathodoluminescence (CL) images reveal that most grains contain inherited cores with homogenous internal structures and magmatic overgrowths with oscillatory zoning (Figure 3a). Analyses on the magmatic domains mostly yielded concordant data (Table S1), with weighted mean ages of 830 ± 5 Ma (mean square weighted deviate (MSWD) = 0.57, n = 17) and 821 ± 6 Ma (MSWD = 0.98, n = 14) for samples 11K07 and 11K97 (Figures 4a and 4b), respectively, which are interpreted as magma crystallization ages. Spot 11K97-06 lies on the discordia line due to mixing of different domains and is excluded from the weighted mean calculation. Analyses on the inherited cores yielded concordant or slightly discordant ages between circa 1.8 and 1.9 Ga, except for two older cores (circa 2.07 Ga for spot 11K07-07 and 2.20 Ga for spot 11K97-22) (Figures 4a and 4b).

Samples 11K94 and 11K99 are garnet- and muscovite-bearing granitoids (Figure 2c). The zircons therein are similar to those in the granodiorite samples in morphology and internal structure, except that inherited cores are larger, and in some cases almost entire grains are inherited cores (Figure 3a). Analyses on the magmatic domains are mostly concordant (Table S1) and yielded weighted mean ages of 830 ± 6 Ma (MSWD = 0.56, n = 16) and 834 ± 6 Ma (MSWD = 0.57, n = 15) for samples 11K94 and 11K99, respectively, indicating a consistent crystallization age within error (Figures 4c and 4d). Spots 11K94-13 and 11K99-12 plot outside the main age group because of strong discordance and are excluded from the calculation. The inherited cores in these two samples are mostly concordant to slightly discordant with ages of circa 1.8–1.9 Ga, except for two slightly older ages (circa 2.2 Ga) from sample 11K94 (Figure 4c).

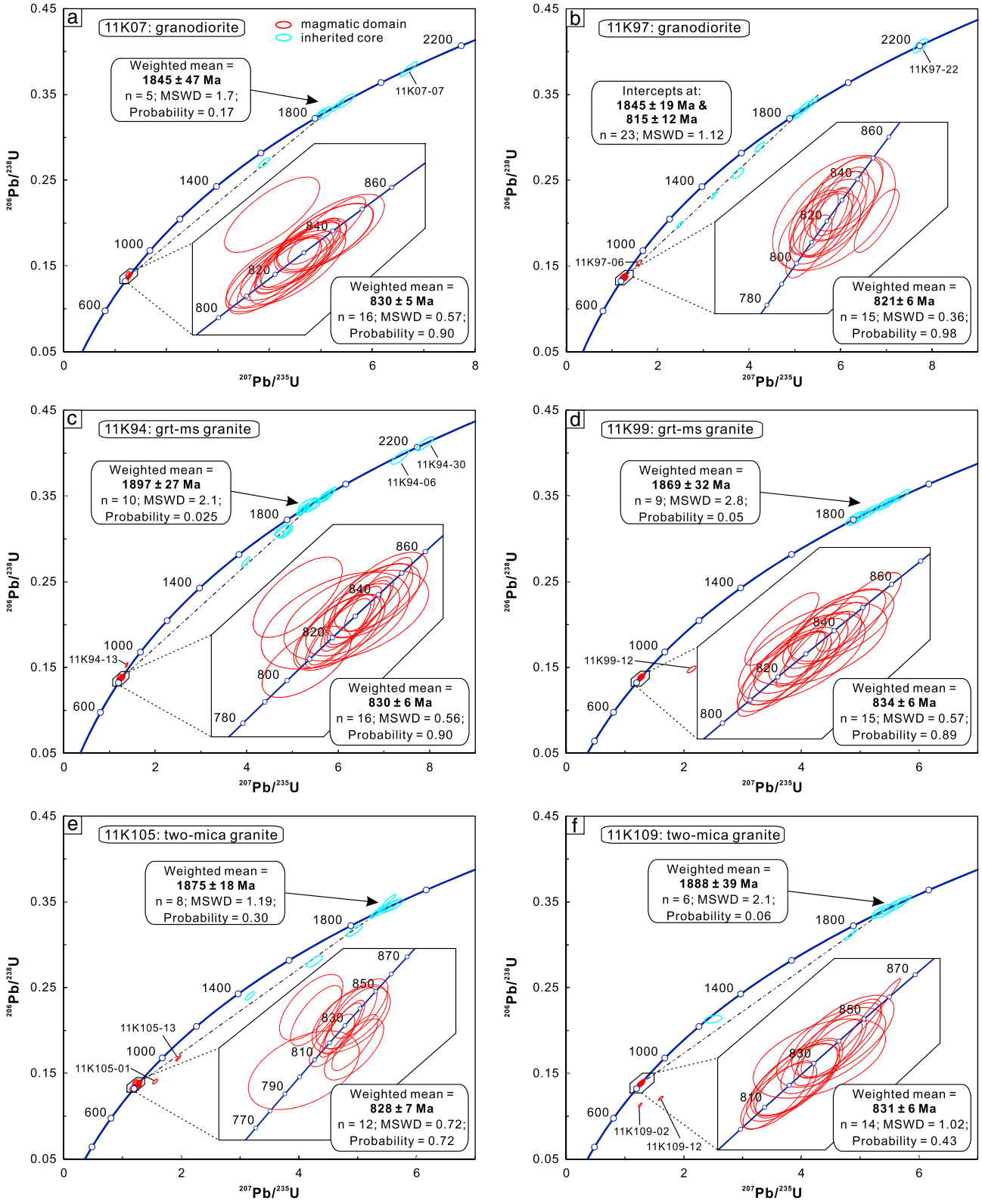

Figure 4. U-Pb concordia diagrams for (a, b) the circa 830–820 Ma granodiorite, (c, d) the garnet-muscovite granite, and (e, f) the two-mica granite in the western Kuruktag area. Note the abundance of circa 1.9–1.8 Ga inherited zircon cores.

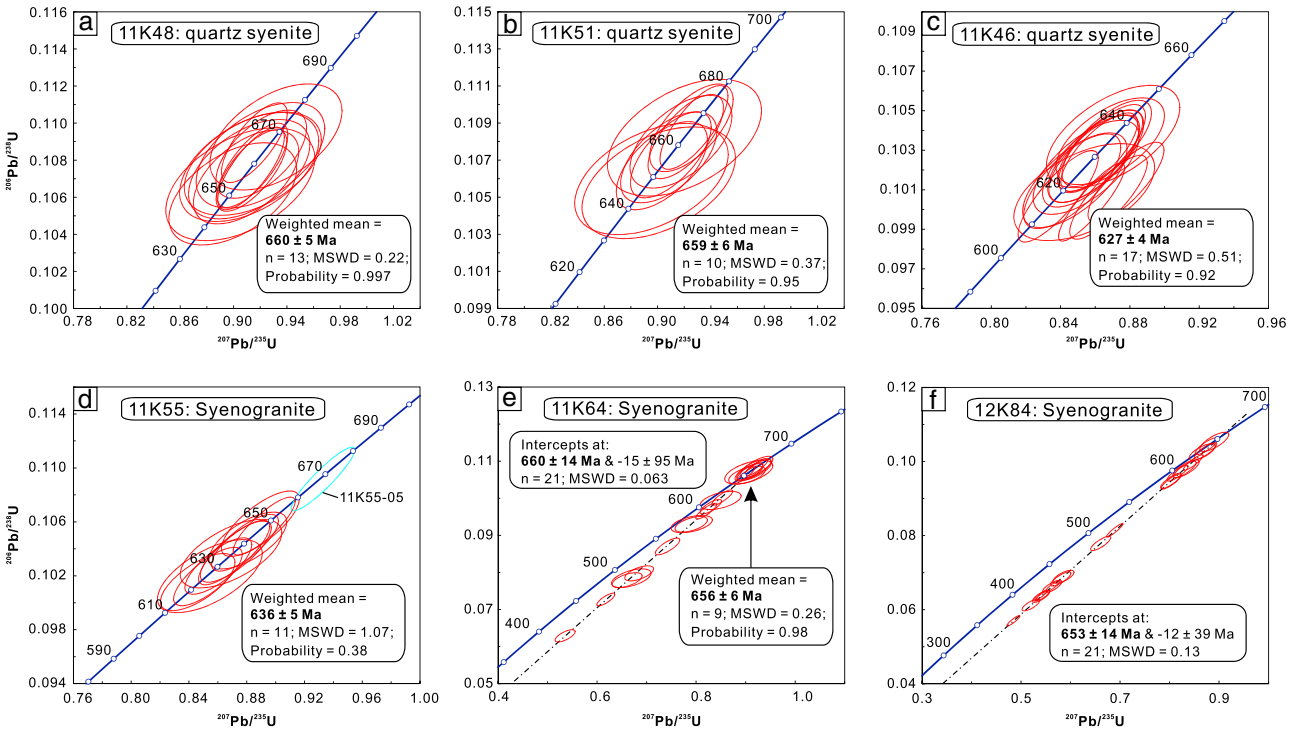

Figure 5. U-Pb concordia diagrams for (a–c) the circa 660–630 Ma quartz syenite and (d–f) the syenogranite in the Korla area.

Samples 11K105 and 11K109 are two-mica granites with zircons mostly showing inherited core-magmatic rim structures (Figure 3a). U-Pb ages for the magmatic domains are mostly concordant (Table S1), yielding weighted mean ages of 828 ± 7 Ma (MSWD = 0.72, n = 11) for sample 11K105 and 831 ± 6 Ma (MSWD = 1.02, n = 14) for sample 11K109, respectively. These data indicate a coeval intrusion age of circa 830 Ma for these two samples. Two analyses from sample 11K105 (11K105-01 and 11K105-13) and two from sample 11K109 (11K109-02 and 11K109-12) are excluded because of strong discordance due to high common Pb or mixing with the cores. Most of the inherited cores in these two samples are dated at circa 1.8–1.9 Ga, with some slightly discordant analyses lying on discordia lines trending to circa 830 Ma.

3.1.2. Late Neoproterozoic Granitoids

Three quartz syenite samples (11K48, 11K51, and 11K46) were dated in this study. Zircons are light yellow, transparent, and euhedral with lengths up to 200 μm and aspect ratios of 1:1–1:3. CL images show that they are mostly oscillatory zoned, and inherited cores are rare (Figure 3b). U-Pb analyses of zircons from samples 11K48 and 11K51 are mostly concordant (Table S1), yielding weighted mean ages of 660 ± 5 Ma (MSWD = 0.22, n = 13) for sample 11K48 and 659 ± 6 Ma (MSWD = 0.37, n = 10) for sample 11K51, respectively, which are interpreted as crystallization ages (Figures 5a and 5b). Three analyses are excluded from sample 11K51: 11K51-10 is highly discordant due to high common Pb content [*Andersen*, 2002]; 11K51-11 is located on the overlap between the magmatic domain and a tiny inherited core; 11K51-04 is slightly younger probably because of radiogenic Pb loss due to its high U and Th contents (Table S1). Zircon U-Pb data for sample 11K46 yielded a younger weighted mean age of 627 ± 4 Ma (MSWD = 0.51, n = 17, Figure 5c), indicating that this sample crystallized about 30 Ma later. Analyses 11K46-10, 11K46-12, and 11K46-13 are discordant due to high common Pb or mixing of magmatic and inherited domains and are excluded from age calculation.

Three syenogranite samples (11K55, 11K64, and 12K84) were also dated. Sample 11K55 contains zircons similar to those in the quartz syenites. Analyses yielded a weighted mean age of 636 ± 5 Ma (MSWD = 1.07, n = 11, Figure 5d). One analysis (11K55-05) is slightly older than the main age group, probably due to inheritance. The other two syenogranites (11K64 and 12K84) also contain zircons similar in size and morphology to those in the quartz syenite samples. However, CL images reveal that these zircons are mostly dark and homogenous, with blurred oscillatory zoning being preserved only in a few grains. They show irregular, CL-bright recrystallized rims or patches along the margins and cracks, but their euhedral morphology remains

unchanged (e.g., grain 11K64-07, Figure 3b). U-Pb analyses demonstrate that the CL-dark zircon domains contain very high Th and U (average Th = 4372 ppm and U = 2148 ppm for sample 11K64, and average Th = 4904 ppm and U = 4050 ppm for sample 12K84); they mostly yielded discordant ages (Table S1). The CL-bright irregular rims or patches yielded much lower Th and U contents and more discordant U-Pb ages. Except for four highly discordant analyses from sample 11K64 (11K64-01, 11K64-06, 11K64-18, and 11K64-23) and two from sample 12K84 (12K84-15 and 12K84-23), the other analyses plot on discordia lines with similar upper intercept ages at 660 ± 14 Ma (MSWD = 0.063, n = 21) and 653 ± 14 Ma (MSWD = 0.13, n = 21), respectively, and a common lower intercept age close to zero (Figures 5e and 5f). The former is consistent with the weighted mean age of 656 ± 6 Ma (MSWD = 0.26, n = 9) of the nine most concordant analyses from sample 11K64. One analysis (12K84-12) yielded a near concordia age of circa 1.9 Ga, reflecting inheritance. These data suggest that both samples crystallized at circa 660 Ma, probably from a high Th-U magma, and experienced radiogenic Pb loss due to radiation damage and metamictization.

3.1.3. Paleozoic Granitoids

Five granodiorite (11K59, 11K71, 11K75, 11K78, and 11K81) and three monzogranite (11K63, 11K68, and 11K83) samples from the Korla area were dated. CL imaging reveals that the zircons are similar in all samples and are characterized by transparent, prismatic, slender crystals, with lengths up to 200 μm and length-to-width ratios of 2:1 to 5:1. Most grains show oscillatory or banded zoning. Patchy or homogenous inherited cores, locally with multiple mantles, are common (Figure 3c). Most magmatic domains yielded concordant ages around circa 420 Ma, with a few yielding consistent $^{206}Pb/^{238}U$ ages but variably older $^{207}Pb/^{235}U$ ages (Figure 6). The eight samples record weighted mean $^{206}Pb/^{238}U$ ages ranging from 417 ± 4 Ma to 421 ± 4 Ma (Figures 6a–6h), consistent within error with each other and those reported by *Ge et al*. [2012a], substantiating that all these granitoids intruded during a short period at circa 420 Ma. Analyses 11K63-08 and 11K81-12 are slightly younger, probably due to radiogenic Pb loss, and were excluded from the age calculations (Figures 6e and 6f). U-Pb ages from the cores vary significantly from sample to sample (Table 1). The analyses within 10% discordance from all the eight samples, when combined with data from *Ge et al*. [2012a], yield a large range from circa 2885 Ma to 459 Ma and define multiple peaks at circa 2.25, 1.86, 0.83, 0.63, 0.51, and 0.46 Ga (figure not shown).

Two monzogranite samples (12K01 and 12K16) from the Paleozoic granitoid belt (Figure 1c) were dated. Zircons in these samples are colorless, transparent, prismatic crystals with lengths up to 300 μm, and aspect ratios between 1:2 and 1:4. They show oscillatory zoning in CL images and locally contain inherited cores with homogeneous or patchy zoning. Analyses of the magmatic domains yielded weighted mean ages of 408 ± 4 Ma (MSWD = 0.72, n = 11, Figure 6i) for sample 12K01 and 406 ± 4 Ma (MSWD = 0.90, n = 13, Figure 6j) for sample 12K16, indicating that they crystallized simultaneously but slightly later than the granitoids in the Korla area. Six analyses of inherited cores from sample 12K16 reveal several age groups, including circa 1.87–1.77, 0.87–0.84, and 0.72 Ga (Table 1).

Two diorite samples (12K09 and 12K33) from the same belt (Figure 1c) were also analyzed. Zircons therein are long prismatic, colorless, transparent crystals with aspect ratios up to 1:7. In CL images they mostly show broad banding (Figure 3c). Only one circa 810 Ma inherited core was detected in sample 12K33, whereas sample 12K09 is core-free. U-Pb analyses of sample 12K09 yielded a weighted mean age of 417 ± 5 Ma (MSWD = 0.46, n = 11, Figure 6k), except for one slightly younger and discordant analysis (12K09-04) probably due to Pb*-loss. Zircon U-Pb data from sample 12K33 yield a weighted mean age of 422 ± 4 Ma (MSWD = 0.27, n = 11, Figure 6l), within error of the previous sample.

3.2. Zircon Hf Isotopic Compositions

3.2.1. Mid-Neoproterozoic Granitoids

The circa 830–820 Ma magmatic zircon domains are characterized by low initial $^{176}Hf/^{177}Hf$ and large negative $\varepsilon Hf(t)$ values (Tables S2 and 1). Comparatively, sample 11K07 has low initial $^{176}Hf/^{177}Hf$ (0.281362–0.281631) and $\varepsilon Hf(t)$ (−31.6 to −22.0), and old two-stage model ages (T_{DM}^2) of 3.1–3.7 Ga, whereas sample 11K94 is more radiogenic and homogeneous, with higher initial $^{176}Hf/^{177}Hf$ (0.281792–0.281936) and $\varepsilon Hf(t)$ (−16.4 to −11.3), and younger T_{DM}^2 values (2.4–2.7 Ga). The other four samples are characterized by initial $^{176}Hf/^{177}Hf$ of 0.281436–0.281837, $\varepsilon Hf(t)$ of −29.1 to −14.7, and T_{DM}^2 values from 2.6 to 3.5 Ga, except for analysis 11K109-15, which has a much lower initial $^{176}Hf/^{177}Hf$ (0.281213) and $\varepsilon Hf(t)$ (−36.8).

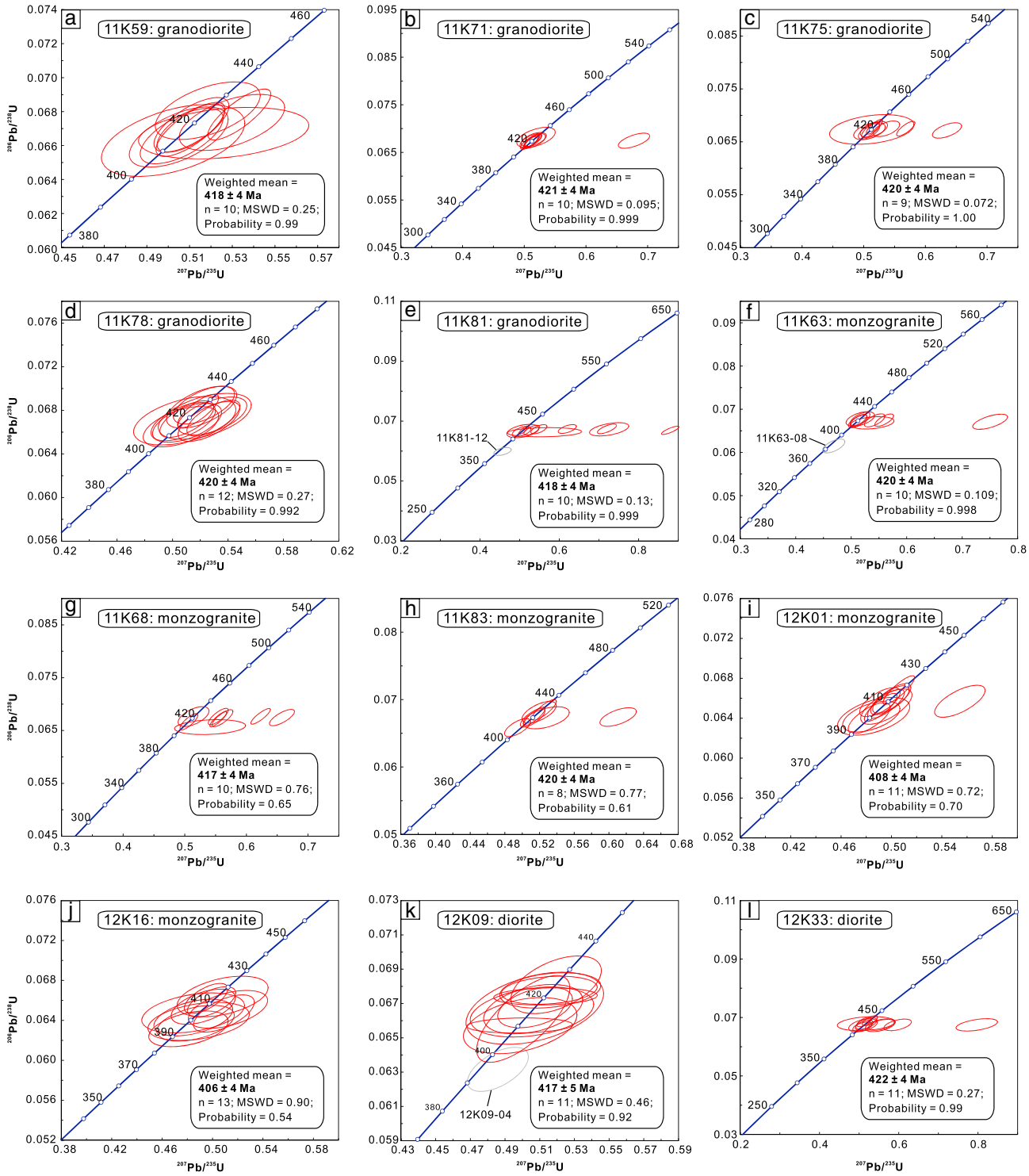

Figure 6. U-Pb concordia diagrams for (a–e) the circa 420–400 Ma granodiorites, (f–j) the monzogranites, and (k, l) the diorites in the western Kuruktag area. Grey ellipses are outliers that are excluded from the weighted mean calculation.

Generally, the Paleoproterozoic inherited cores show lower initial $^{176}Hf/^{177}Hf$ but more positive $\varepsilon Hf\ (t)$ values than the corresponding magmatic domains for each sample. However, both domains show similar ranges of T_{DM}^2 values (Figure 8a) and can be fitted to an evolutionary array with a T_{DM}^2 of 2.5–3.5 Ga using $^{176}Lu/^{177}Hf = 0.015$ (Figures 7a–7c).

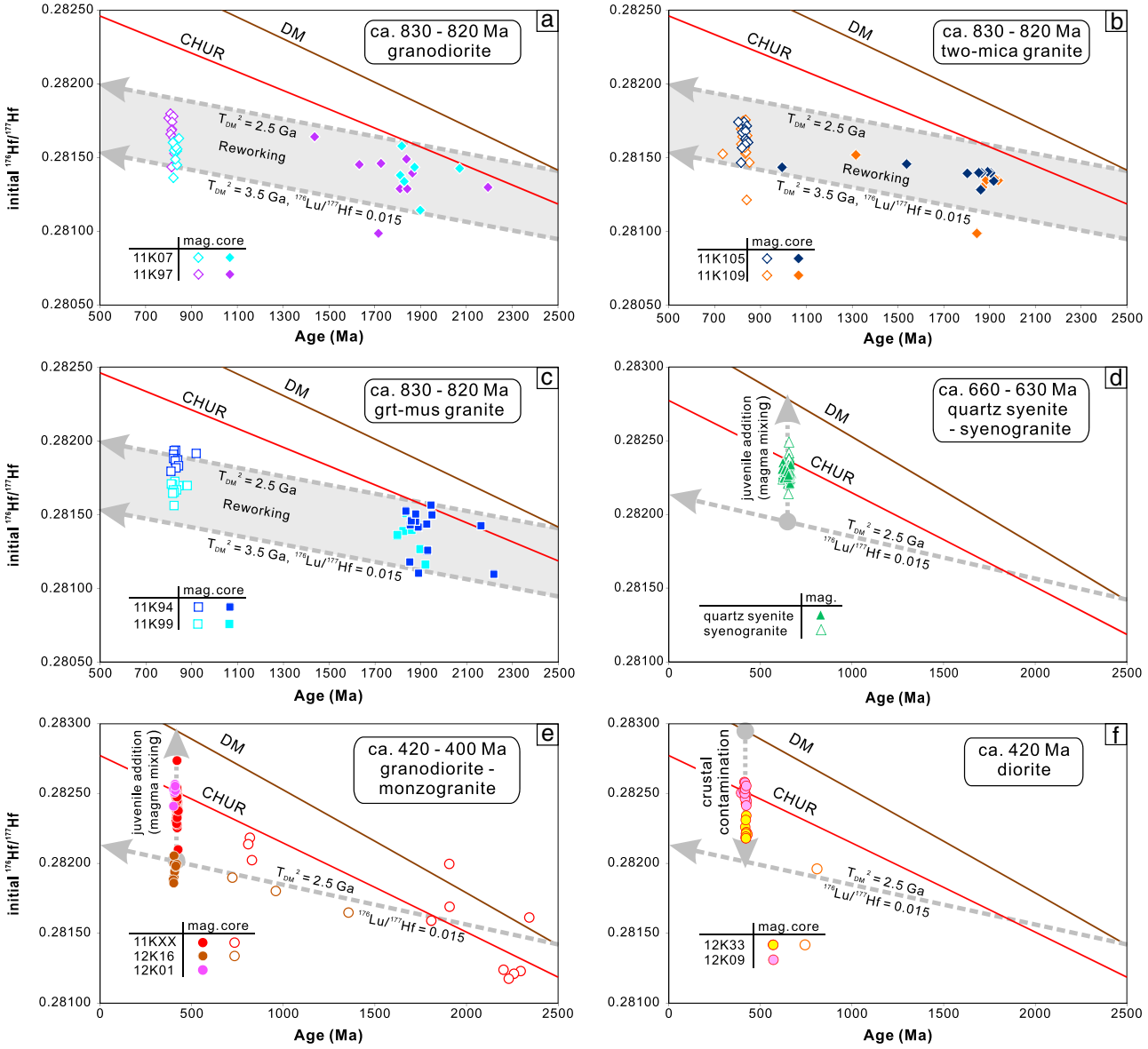

Figure 7. Initial $^{176}Hf/^{177}Hf$ versus U-Pb age plots for the granitoids from the western Kuruktag area. Note that the magmatic zircons and the inherited cores in the (a–c) circa 830–820 Ma granitoids broadly fall on the same evolutionary array of 2.5–3.5 Ga crust using a $^{176}Lu/^{177}Hf$ value of 0.015, whereas the (d) circa 660–630 Ma, and (e) circa 420–400 Ma zircons have initial $^{176}Hf/^{177}Hf$ values mostly plotting above this array and ranging across the chrondritic reservoir (CHUR) line. (f) Two diorite samples having different zircon Hf isotopic compositions. Grt = garnet and mus = muscovite.

3.2.2. Late Neoproterozoic Granitoids

Three quartz syenite samples (11K48, 11K51, and 11K46) yielded similar zircon Hf isotopic compositions, with initial $^{176}Hf/^{177}Hf$ of 0.282199–0.282352, $\varepsilon Hf(t)$ of −5.7 to −0.9, and T_{DM}^2 of 1.6–1.9 Ga (Table 1). The syenogranite sample 11K55 has similar zircon Hf compositions ($\varepsilon Hf(t) = -4.8$ to -1.9) to the quartz syenites. The other two syenogranites (11K64 and 12K84) with discordant U-Pb ages and high Th-U contents yielded more variable $^{176}Hf/^{177}Hf$ values, but these are not correlated with the discordance of U-Pb ages, suggesting that the Lu-Hf system remained closed, whereas the U-Pb system was open to radiogenic Pb loss. Using the crystallization ages, the calculated $\varepsilon Hf(t)$ values vary from −3.8 to +4.5 for sample 11K64 and from −7.9 to −1.2 for sample 12K84. Collectively, the circa 660–630 Ma granitoids are more juvenile in Hf isotopic composition than the circa 830–820 Ma granitoids, suggesting addition of juvenile material during magma genesis.

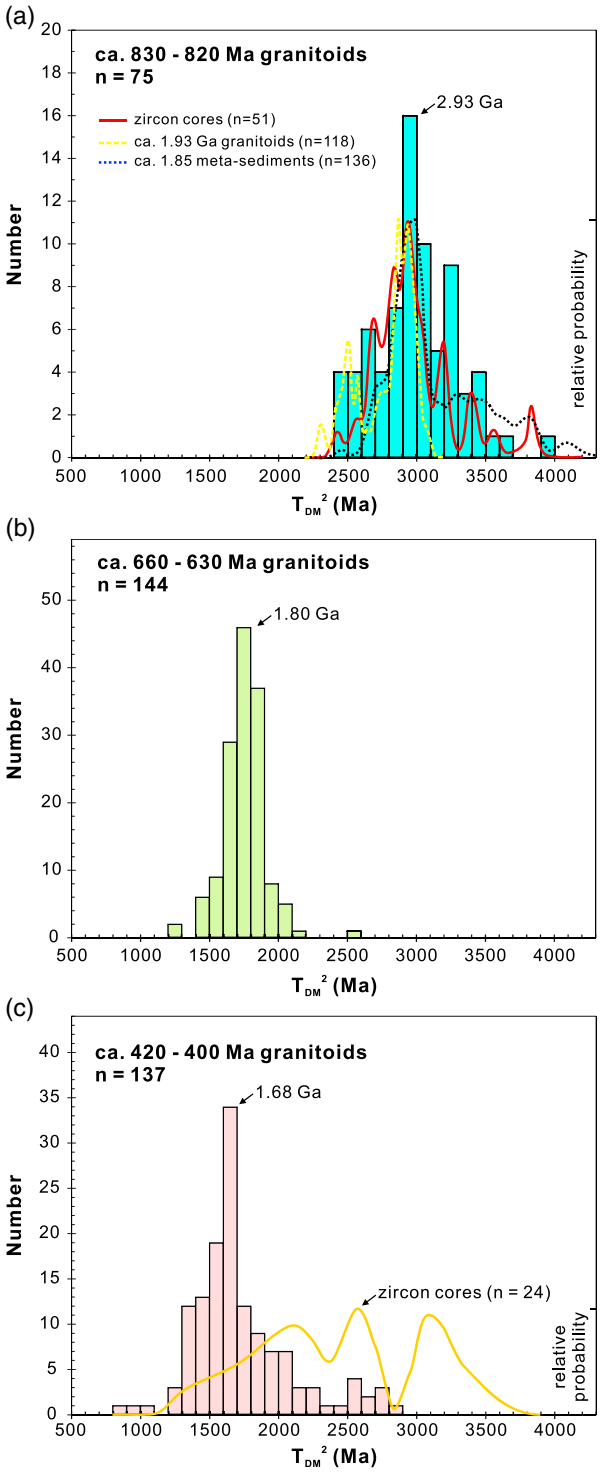

Figure 8. Histogram of two-stage Hf model ages (T_{DM}^2) for (a) the circa 830–820 Ma, (b) the circa 660–630 Ma, and (c) the circa 420–400 Ma granitoids. The $^{176}Lu/^{177}Hf$ value of 0.015 is used for calculation. Data from *Ge et al.* [2012a, 2012b] are included in Figures 8c and 8b, respectively. The solid curves in Figures 8a and 8c show the relative probability of T_{DM}^2 of zircon cores in magmatic zircons. The relative probability curves of T_{DM}^2 for the circa 1.93 Ga granitoids (dashed line, data from *Lei et al.* [2013] and our unpublished data) and circa 1.85 Ga metasedimentary rocks (dotted line, data from *Ge et al.* [2013b]) are shown in Figure 8a for comparison.

3.2.3. Paleozoic Granitoids

Zircon Hf isotopic compositions of the 12 Paleozoic granitoids vary from sample to sample (Table 1). The eight granodiorite and monzogranite samples from the Korla area have an overall range of εHf (t) values of −14.6 to +8.0, corresponding to initial $^{176}Hf/^{177}Hf$ of 0.282099 to 0.282735 and T_{DM}^2 of 0.9–2.3 Ga (Table 1). The largest variation within an individual sample is about 15 epsilon units (−14.6 to +1.1 for sample 11K78 and −6.5 to +8.0 for sample 11K83). Such a huge variation is similar to that previously documented in the same area [*Ge et al.*, 2012a]. The inherited cores also yield variable εHf (t) (−8.2 to +15.2), but they generally have much lower initial $^{176}Hf/^{177}Hf$ (0.281029 to 0.282024) and older T_{DM}^2 (1.6–3.2 Ga, Figure 8c) than the magmatic domains, implying that they may not be residual from the magma source but xenocrysts entrained during magma ascent. Sample 12K01 has a similar zircon Hf isotopic composition to the granodiorites-monzogranites in the Korla area. However, sample 12K16 has more negative εHf (t) (−23.4 to −16.5), lower initial $^{176}Hf/^{177}Hf$ (0.281809–0.282055), and older T_{DM}^2 model ages (2.42–2.85 Ga) than the other samples (Table 1), indicating a dominant contribution from ancient continental crust. The two diorite samples have different zircon Hf isotopic compositions (Figure 7f) with εHf (t) varying from −3.4 to +2.5 for sample 12K09 and from −11.7 to −2.9 for sample 12K33, also implying involvement of both juvenile and ancient crustal material.

3.3. Whole-Rock Geochemistry

3.3.1. Mid-Neoproterozoic Granitoids

The hornblende- and/or epidote-bearing granodiorite samples show variable SiO_2 contents (63.3–70.0 wt.%, Table S3), which negatively correlate with Al_2O_3, CaO, $Fe_2O_3^T$, TiO_2, MgO, P_2O_5, Sr, and light rare earth element (LREE), and positively correlate with K_2O and Rb (figures not shown). They have high-Na_2O contents (3.9–5.4%) and Na_2O/K_2O ratios (1.47–5.10), plotting in the granodiorite and granite fields in the SiO_2 versus $Na_2O + K_2O$ diagram (Figure 9a) and the TTG fields on the Or-An-Ab diagram (Figure 9b). They are metaluminous to

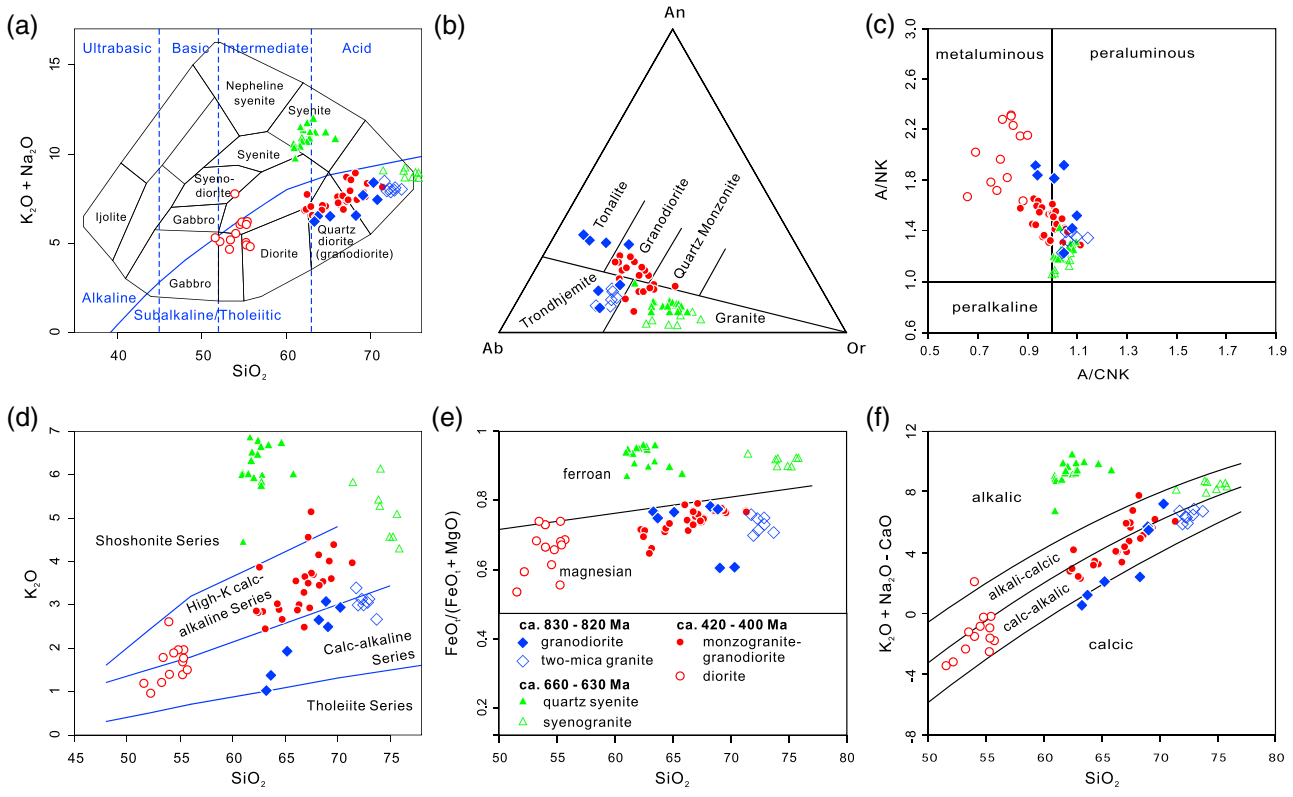

Figure 9. Chemical classification diagrams for the granitoids from the western Kuruktag area. (a) TAS diagram [after *Cox et al.*, 1979], (b) An-Ab-Or diagram [after *O'Connor*, 1965], (c) A/CNK-A/NK diagram [after *Shand*, 1943]; (d) SiO_2-K_2O [after *Peccerillo and Taylor*, 1976], (e) $FeO_t/(FeO_t + MgO)$ and (f) $(K_2O + Na_2O - CaO)$ versus SiO_2 diagram [after *Frost et al.*, 2001].

peraluminous (molar $Al_2O_3/(CaO + Na_2O + K_2O)$) (A/CNK) = 0.92–1.10, Figure 9c) and show calc-alkaline and magnesian calc-alkaline to calcic affinities (Figures 9d–9f). These major element features are similar to those of Archean TTG gneisses or modern adakites. However, they show variable Y (10. 9–38.7 ppm) and Yb (1.26–4.38 ppm) contents and Sr/Y (4.2–89.8) and $(La/Yb)_N$ (5.1–19.4) ratios, covering the range of typical TTG and adakitic rocks and normal calc-alkaline granitoids. On the REE and trace element diagrams (Figures 10a and 10b), they mostly show positive Eu anomalies and variable enrichments in LREE, Ba, Sr, and depletion in Nb-Ta, P, and Ti.

The two-mica granite samples have relatively high SiO_2 (71.7–73.7%) and Na_2O (4.8–5.3%) but low TiO_2 (0.12–0.14%) and P_2O_5 (0.03–0.04%) contents (Table S3). They plot in the granite field in the SiO_2 versus $Na_2O + K_2O$ diagram (Figure 9a) and the trondhjemite field on the Or-Ab-An diagram (Figure 9b). The A/CNK values (1.03–1.14) indicate that they are weakly peraluminous (Figure 9c). These samples belong to the calc-alkaline or magnesian calc-alkaline to calcic series (Figures 9d–9f). They are similar to the granodiorite samples in terms of REE and trace element patterns, except for their more pronounced positive Eu anomalies and stronger depletion in P (Figures 10a and 10b).

3.3.2. Late Neoproterozoic Granitoids

The quartz syenites contain low SiO_2 (61.0–63.2%) and MgO (0.33–0.69%) but high K_2O (4.4–7.6%), Na_2O (4.4–5.2%), $Fe_2O_3^T$ (3.4–5.0%), and Al_2O_3 (18.2–19.0%) (Table S3), plotting in the syenite field (Figure 9a). They are weakly peraluminous (Figure 9c) and plot in shoshonitic and ferroan, alkalic fields (Figures 9d–9f). These samples are characterized by variable enrichment in LREE and weak to moderate positive Eu anomalies, except for sample 11K53 with the highest REE and a pronounced negative Eu anomaly, probably due to plagioclase fraction, and sample 10T67 with depleted middle-REE and a pronounced positive Eu anomaly, probably due to residual hornblende (Figure 10c). Most samples are relatively enriched in Ba, K, Zr, and Hf and depleted in Nb-Ta, Ti, and Sr (Figure 10d).

The syenogranite samples are characterized by high SiO_2 (74.5–75.8%), K_2O (4.3–6.1%), and Na_2O (3.0–4.3%), and low Al_2O_3 (12.2–14.0%), CaO (0.29–0.89%), MgO (0.12–0.21%), and P_2O_5 (0.01–0.04%) contents (Table S3).

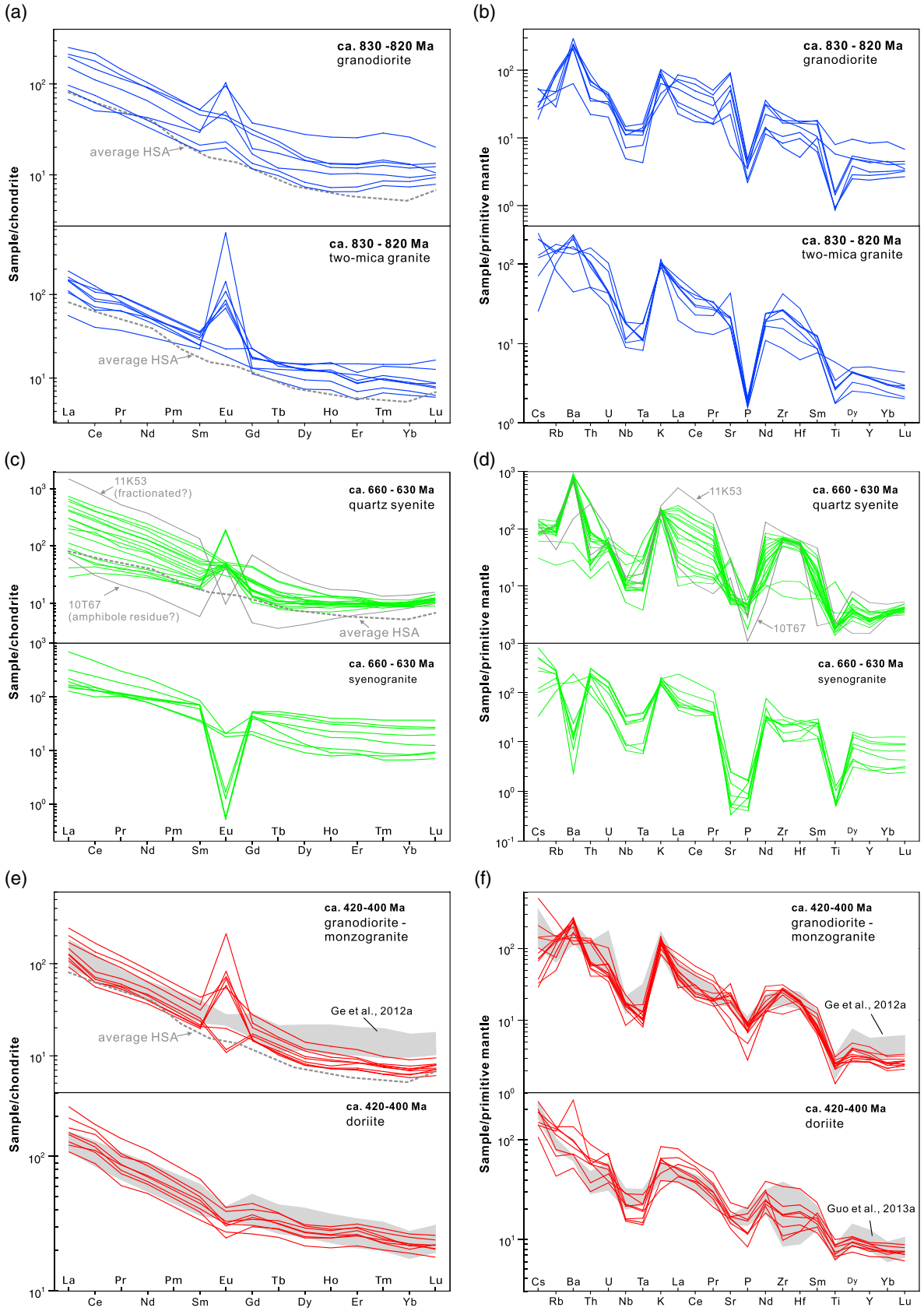

Figure 10

They are weekly peraluminous (A/CNK = 1.00–1.07) (Figure 9c) and belong to the high-K calc-alkaline to shoshonitic series and the ferroan alkali-calcic series (Figures 9d–9f). On the REE diagram, they show variable enrichment in LREE and have weak to large negative Eu anomalies. They are variably enriched in Cs, Rb, and K with depletion in Nb-Ta, Ti, Ba, Sr, and P (Figure 10d).

3.3.3. Paleozoic Granitoids

The circa 420–400 Ma granodiorite-monzogranite samples have moderate SiO_2 (66.5–71.4%), Na_2O (3.5–4.9%), and K_2O (2.4–5.1%) contents (Table S3), plotting in the granite-granodiorite fields (Figures 9a and 9b). They are metaluminous to weakly peraluminous (A/CNK = 0.98–1.09, Figure 9c). These rocks mostly belong to the high-K calc-alkaline and magnesian calc-alkalic to alkali-calcic series (Figures 9d–9f) and are characterized by strong LREE enrichment, with either weakly negative or strong positive Eu anomalies (Figure 10e). They have lower heavy rare earth element (HREE) contents than those previously analyzed from the same area [*Ge et al*., 2012a]. Nb-Ta, Ti, and P are relatively depleted, whereas Ba and K are variably enriched (Figure 10f).

The contemporaneous diorites are intermediate (SiO_2 = 51.5–55.7%), with variable but high MgO (2.7–6.8%), Cr (12.7–147 ppm), and Ni (7.51–48.6 ppm) contents (Table S3). They are strongly metaluminous (Figure 9c) and mostly belong to the calc-alkaline series and magnesian calc-alkalic series (Figures 9d–9f). On REE and trace element distribution diagrams, they are characterized by moderate LREE enrichment and weak negative Eu anomalies (Figure 10e). They are enriched in Cs, Ba, and K, and depleted in Nb-Ta, Ti, Sr, and P, and also in Zr and Hf for two samples (Figure 10f).

4. Discussion

4.1. Magma Source(s) and Melting Conditions

4.1.1. Mid-Neoproterozoic Granitoids

It is generally accepted that the primary magma composition of granitoids is controlled by magma source and melting conditions (pressure, temperature, and fluid availability), which are in turn correlated with tectonic settings. Our data provide the first reliable crystallization ages for the mid-Neoproterozoic granitoid plutons in the western Kuruktag area and indicate that these rocks were intruded over a relatively short period from circa 834 to 821 Ma, slightly older than those in the central and eastern Kuruktag dated at circa 826–785 Ma, with minor intrusions at circa 760 Ma, 754 Ma, and 735 Ma [e.g., *Zhang et al*., 2007, 2012a; *Shu et al*., 2011; *Long et al*., 2011a; *Cao et al*., 2011]. These granitoids are mostly Na_2O rich, similar to TTG and adakite in major element composition. Experimental studies have documented that such sodic granitoids are most likely produced by partial melting of hydrated mafic rocks (amphibolite or eclogite) [e.g., *Wolf and Wyllie*, 1994; *Sen and Dunn*, 1994; *Patiño Douce and Beard*, 1995; *Rapp et al*., 1995; *Qian and Hermann*, 2013]. Their old Hf model ages (circa 2.5–3.5 Ga) suggest a protolith of Archean mafic lower crust (Figure 8a). However, these granitoids contain abundant circa 1.8–1.9 Ga inherited zircons with Hf isotopic compositions that fit the same evolutionary array of the circa 2.5–3.5 Ga Archean crust using a $^{176}Lu/^{177}Hf$ value of 0.015 (Figures 7a–7c and 11). This relationship implies that the Archean protolith was probably affected by a late Paleoproterozoic metamorphic event and was reworked again during the mid-Neoproterozoic. This interpretation is consistent with the circa 1.9–1.8 Ga regional metamorphism in this area [e.g., *Zhang et al*., 2012b; *Ge et al*., 2013b] and the internal structure of the inherited zircons. The Hf isotopic features also indicate limited depleted mantle contribution to the magma source, consistent with the low MgO, Cr, and Ni contents of these granitoids. The granitoids in the central Kuruktag area also exhibit large negative whole-rock εNd and zircon εHf values and were probably derived from similar Archean mafic lower crust of the northern Tarim Craton [*Zhang et al*., 2007, 2012a; *Long et al*., 2011a; *Cao et al*., 2011].

Given a similar source composition, the Yb and Y content of granitic melts, and thus other REE to Yb ratios, are mainly controlled by residual garnet during partial melting, whereas the Sr content and Eu anomaly are mainly controlled by residual plagioclase. As the abundance of residual garnet and plagioclase is pressure-dependent, these parameters can in turn be used to infer the melting pressure or depth [e.g., *Martin et al*., 2005]. Here we

Figure 10. (a, c, and e) REE and (b, d, and f) trace element diagrams for the granitoids from the western Kuruktag, north Tarim. The circa 830–820 Ma granitoids (Figures 10a and 10b), the circa 660–630 Ma granitoids (Figures 10c and 10d), the circa 420–400 Ma granitoids (Figures 10e and 10f). Normalization values after *Sun and McDonough* [1989].

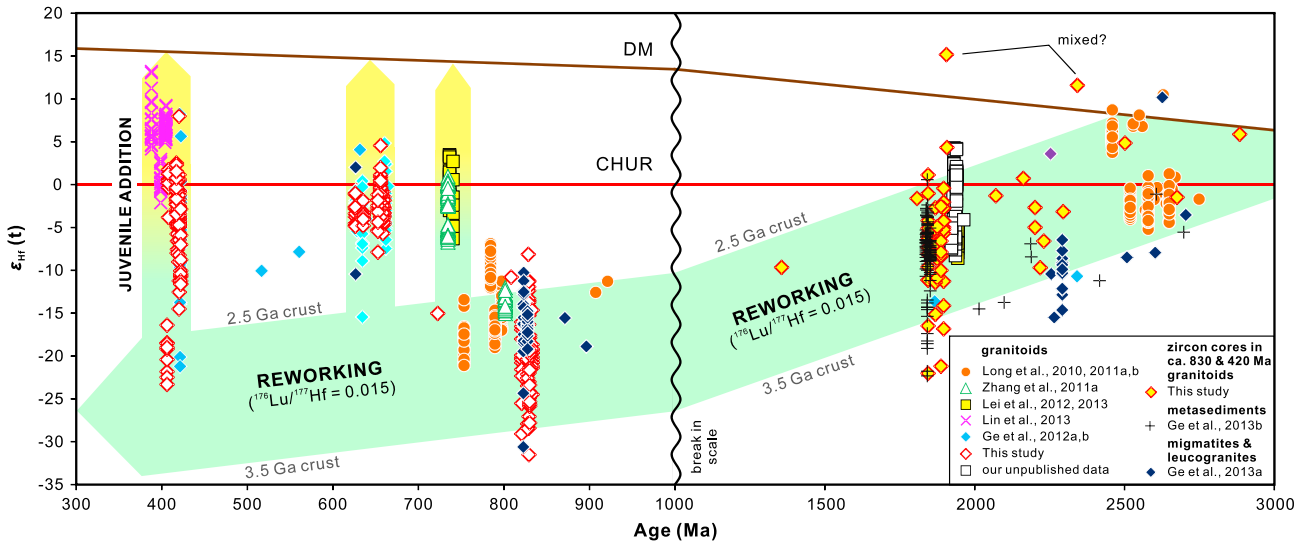

Figure 11. Zircon εHf (*t*) versus age plot of the Neoproterozoic and Paleozoic (left) granitoids and (right) basement rocks in the northern Tarim Craton. The circa 830–820 Ma magmatic zircons and their cores broadly fall on the same evolutionary array as the circa 2.5–3.5 Ga crust defined by most zircons from the basement rocks, suggesting they were derived from crustal reworking without significant contribution from the depleted mantle. In contrast, zircons from the circa 740 Ma, 660–630 Ma, and 420–400 Ma granitoids mostly plot above this array and were probably formed by magma mixing between crustal materials with juvenile magma derived from the contemporary depleted mantle.

use Ho/Yb ratios as a proxy of residual garnet (Figure 12a), because both Ho and Yb are HREE and are less affected by source enrichment and residual amphibole than the commonly used La/Yb, Sm/Yb, and Gd/Yb ratios. Generally, only the maximum Ho/Yb ratio (i.e., the maximum garnet abundance in the residue assuming similar magma source) can provide a minimum constraint on melting depth and crustal thickness for a given time and area.

The circa 834–821 Ma granitoids in western Kuruktag have variable Sr, Y, and Yb contents and Sr/Y and $(Ho/Yb)_N$ ratios, with about half of the samples falling within the definition of adakite (Sr > 400 ppm, Y < 18 ppm, and Yb < 1.9 ppm) [*Defant and Drummond*, 1990; *Martin et al*., 2005], implying partial melting at least partly in the garnet stability field (>10 kbar). The distinct positive Eu anomalies for most samples may imply limited plagioclase residue in the source region and possibly some plagioclase accumulation. Therefore, we propose that these sodic granitoids were formed by partial melting of Archean mafic lower crust in a normal to slightly thickened crust. The compositional differences between the high SiO_2, peraluminous two-mica granite and the low SiO_2, metaluminous granodiorite may have resulted from low and high degrees of partial melting, respectively. The slightly younger, circa 826–785 Ma adakitic granitoids in the central Kuruktag have much higher Ho/Yb ratios [*Zhang et al*., 2007; *Long et al*., 2011a] (Figure 12a) and may imply rapid crustal thickening in the Kuruktag area.

As zircon is one of the earliest crystallization phases in granitoids, zircon saturation temperature can provide constraints on the primary magma temperature [*Watson and Harrison*, 1983; *Hanchar and Watson*, 2003; *Miller et al*., 2003]. The calculated average zircon saturation temperature (T_{Zr}) is 770°C for the granodiorite and 826°C for the two-mica granite in west Kuruktag (Figure 12b). The slightly younger granitoids in central and eastern Kuruktag [*Zhang et al*., 2007, 2012a; *Long et al*., 2011a; *Cao et al*., 2011] yielded even lower values (average 764 and 715°C, respectively, Figure 12b). Note that these values are maximum estimates because the presence of abundant inherited zircons indicates that the primary magmas were Zr oversaturated [*Miller et al*., 2003]. Thus, the primary magma temperature for most granitoids might be significantly lower than that is required for considerable dehydration melting of mafic rocks (amphibolite), as determined by experimental studies (at least circa 800–850°C) [e.g., *Wolf and Wyllie*, 1994; *Sen and Dunn*, 1994; *Patiño Douce and Beard*, 1995; *Rapp et al*., 1995; *Qian and Hermann*, 2013]. It is therefore inferred that these granitoids were probably produced at relatively low temperature by fluid-present partial melting due to influx of external fluids, rather than by dehydration melting due to heating [*Miller et al*., 2003].

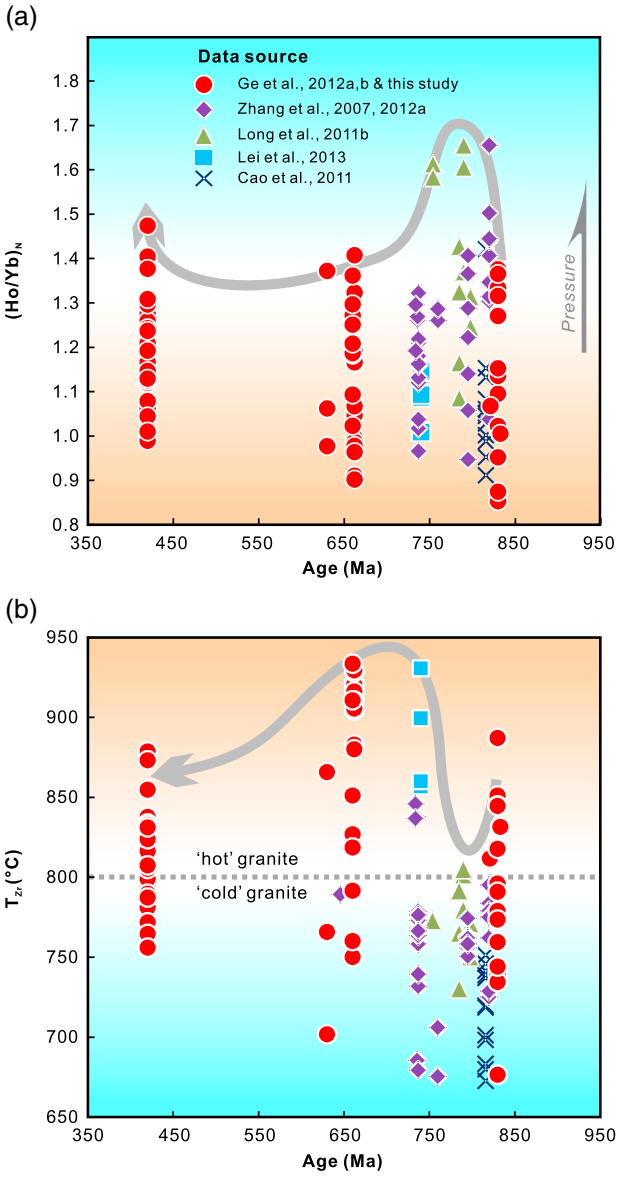

Figure 12. (a) $(Ho/Yb)_N$ ratio versus age and (b) Zircon saturation temperature (T_{Zr}) [*Watson and Harrison*, 1983] versus age diagrams for the granitoids from the Kuruktag area, north Tarim Craton. Normalization values after *Sun and McDonough* [1989]. The boundary between "hot" granite and "cold" granite (800°C) in Figure 12b is after *Miller et al.* [2003]. Note that it is the maximum Ho/Yb ratio (i.e., the maximum garnet abundance in the residue assuming similar magma source) that provides a minimum constraint on melting depth and crustal thickness.

4.1.2. Late Neoproterozoic Granitoids

The circa 660–630 Ma quartz syenite and syenogranite are coeval and spatially associated with mafic dikes [*Zhu et al.*, 2008, 2011b] and gabbroic plutons (our unpublished data). However, these rocks have different major and trace element characteristics and do not show coherent trends on the Harker diagrams (not shown), excluding a common origin via assimilation and fractional crystallization. Both the syenogranite and quartz syenite are characterized by low MgO, Cr, and Ni contents and mostly negative zircon εHf (t) values, suggesting a dominantly crustal origin. However, their highly variable zircon Hf isotopic compositions imply that they were probably affected by magma mixing with a depleted mantle-derived mafic magma [see *Ge et al.*, 2012b]. This is supported by the wide occurrence of mafic enclaves and evidence for magma mingling in the field.

Comparatively, the syenogranite samples are characterized by high SiO_2, moderate K_2O, $K_2O + Na_2O$ with $Na_2O/K_2O < 1$, and low Al_2O_3, CaO, Ba, Eu*, Sr, and Sr/Y, consistent with dehydration melting of intermediate rocks (tonalite) at a relatively shallow crustal level, leaving a plagioclase-rich, garnet-free granulitic residue (<8 kbar) [e.g., *Patiño Douce and Beard*, 1995; *Singh and Johannes*, 1996]. The suggested magma source and melting conditions are similar to those proposed for some A-type granites [*Patiño Douce*, 1997]. The syenogranites, however, have low Ga, Zr, Nb, Ce, Y, and Zn contents relative to typical A-type granite [*Whalen et al.*, 1987]. This is probably due to lower magma temperature (760–866°C), as estimated using the zircon saturation thermometer [*Watson and Harrison*, 1983], than that of A-type granite (usually >900°C).

In comparison, the quartz syenite contains lower SiO_2, higher Al_2O_3, total alkalis ($N_2O + K_2O$), CaO, MgO, and FeO/MgO, suggesting that the protolith was more mafic. *Xiao and Clemens* [2007] carried out dehydration melting experiments on a potassic basaltic andesite (shoshonite) at 1050–1075°C and 1.5–2.5 GPa. The resulting melts were syenitic, similar in major element composition to the present samples. The melts, however, were coexisting with garnet-rich and plagioclase-free residues under the high experimental pressure, thus were expected to have adakitic trace element features [*Xiao and Clemens*, 2007]. In contrast, most quartz syenite samples in this study exhibit low Sr and thus low Sr/Y, suggesting the presence of plagioclase in the residue. Moreover, these samples exhibit flat, even positive, middle rare earth element (MREE) to HREE slopes, which may be due to the influence of residual amphibole, rather than garnet, although a few samples show high

$(Ho/Yb)_N$ ratios, and the presence of garnet residue cannot be completely ruled out. The estimated zircon saturation temperature is 881–949°C (average 914°C, except 702 and 751°C for samples 11K46 and 11K48, respectively), lower than that used by *Xiao and Clemens* [2007] but high enough for considerable dehydration melting of hydrated mafic rocks, implying that influx of external water was unnecessary.

4.1.3. Paleozoic Granitoids

The circa 420–400 Ma monzogranites-granodiorites are hornblende-bearing, metaluminous to weakly peraluminous, I-type granitoids (Figure 10f). Their low MgO, Cr, and Ni, and moderate SiO_2, Al_2O_3, total alkalis ($N_2O + K_2O$), and Na_2O/K_2O ratios, as well as the dominantly negative zircon εHf (t) values, suggest that they were mostly derived from a crustal protolith, probably of mafic to intermediate composition (amphibolite or tonalite). However, a depleted mantle component must have been involved, probably via magma mixing, in order to cause the large, continuous variations in zircon Hf isotopic composition, because the most radiogenic value (εHf (t) = +8.2, T_{DM}^2 = 0.89 Ga) has not been found in older rocks in this area. Notably, the samples presented in this study have higher Sr but lower Yb and Y contents, and steeper REE slopes similar to average high-silica adakite [*Martin et al*., 2005] (Figure 10e), than those reported previously [*Ge et al*., 2012a]. Based on their Sr, Y, and Yb contents, 6 of the 12 samples in this study can be grouped as adakite (Sr $>$ 400 ppm, Y $<$ 18 ppm, and Yb $<$ 1.9 ppm) [*Defant and Drummond*, 1990; *Martin et al*., 2005]. These adakite-like samples exhibit intermediate SiO_2 and Mg# relative to the other non-adakitic samples, suggesting that they cannot be generated by fractionation crystallization or magma mixing. Therefore, at least some of the Paleozoic granitoids formed in the garnet stability field ($>$10 kbar). The zircon saturation temperatures of the Paleozoic granitoids range from 764 to 855°C (average 810°C, Table S3). As the presence of abundant inherited zircons indicates Zr oversaturation, the primary magma temperature should be lower than these values, which may not be high enough for dehydration melting of a mafic to intermediate rocks at lower crustal conditions [e.g., *Wolf and Wyllie*, 1994; *Sen and Dunn*, 1994; *Rapp et al*., 1995]. Therefore, influx of external fluids can be inferred.

The associated Paleozoic diorites are characterized by low SiO_2 and high MgO, Mg#, Cr, Co, and Ni, indicating a likely mantle origin. With decrease in the Mg#, there is a corresponding decrease in FeO, Al_2O_3, CaO, Cr, Co, and Ni (figures not shown), suggesting fractional crystallization of olivine, pyroxene, and plagioclase. The latter is consistent with weak negative Eu anomalies of some samples. The zircon εHf (t) is also variable, but as zircon is a late crystallization phase in mafic to intermediate magma, such large variation is probably due to high-level crustal contamination, rather than source enrichment. The diorites are depleted in Nb-Ta and Ti and also in Zr and Hf for samples 11K11 and TKD23-01-1 [*Guo et al*., 2013a]. Although the rocks may not represent primary magmas and the negative Nb-Ta-Ti anomalies may result from crustal assimilation, as indicated by zircon Hf isotopic data, it is generally accepted that negative Zr-Hf anomalies cannot be generated by such processes, because crustal rocks are usually not depleted in these two elements. This implies that the depletion of high field strength elements (HFSE) in these rocks is probably a primary feature of the parent magma, which was likely generated by low-temperature hydrous melting of depleted lithospheric mantle wedge due to influx of subduction-related fluids/melts.

4.2. Neoproterozoic Magmatism: Mantle Plume or Accretionary Orogeny?

The most popular dynamic model for the Neoproterozoic magmatism is two episodes of mantle plume activity at circa 825–800 and 780–740 Ma possibly related to the breakup of Rodinia [e.g., *Xu et al*., 2005; *Zhang et al*., 2012a; *Long et al*., 2011a; *Shu et al*., 2011], which was first proposed by *Li et al*. [1999] for coeval events in South China. However, no direct evidence of mantle plume activity, e.g., komatiite or high-Mg basalt, continental flood basalt, OIB, etc., has been found in northern Tarim. Moreover, the circa 830–790 Ma igneous rocks are dominated by granitoids derived from reworking of Archean mafic lower crust with little mantle contribution. Minor amounts of mafic-ultramafic-carbonatitic rocks were argued to be products of mantle plume activity [e.g., *Zhang et al*., 2007; *Ye et al*., 2013], but these rocks are consistently enriched in LREE and large-ion lithophile element (LILE), and depleted in Nb-Ta-Ti, locally also in Zr-Hf, thus are most likely derived from partial melting of a metasomatized lithospheric or asthenospheric mantle, triggered by subduction-related fluids/melts, rather than plume-related heating. No deeper or hotter mantle-derived material (e.g., OIB or high-Mg basalts, respectively) has been documented during this period in northern Tarim.

In contrast, blueschists and associated metasedimentary rocks in the Aksu area, NW Tarim (Figure 1b), are unconformably overlain by a Marinoan-aged (circa 635 Ma) glacial diamictite (Yulmenack Formation) and provide robust evidence for Neoproterozoic subduction and accretion [*Liou et al*., 1989, 1996; *Nakajima et al*., 1990;

Zheng et al., 2010; *Zhu et al*., 2011a; *Yong et al*., 2012]. The Aksu blueschist was previously interpreted as evidence for an early Neoproterozoic interior accretionary orogen related to the assembly of Rodinia [*Li et al*., 2008]. This interpretation is mainly based on several contentious zircon U-Pb ages (ranging from 810 to 755 Ma) from mafic dikes that penetrate the Aksu blueschists [*Chen et al*., 2004; *Zhan et al*., 2007; *Zhang et al*., 2009a] and is inconsistent with the circa 750–700 Ma metamorphic ages obtained by Rb-Sr, K-Ar [*Nakajima et al*., 1990; *Liou et al*., 1989], and $^{40}Ar/^{39}Ar$ techniques [*Yong et al*., 2012], as well as the circa 730 Ma maximum depositional ages for the associated metasedimentary rocks given by detrital zircon dating [*Zhu et al*., 2011a]. *Zheng et al*. [2010] obtained a whole-rock Sm-Nd isochron age of 890 ± 23 Ma for mafic schists with enriched mid-ocean ridge basalt (MORB) affinity in the Aksu area. This is similar to the U-Pb ages (circa 1000–880 Ma) of zircon cores from the Paleozoic (circa 465 Ma) Beishan eclogite close to northeastern margin of Tarim, which also has a protolith of MORB affinity [*Yang et al*., 2006; *Liu et al*., 2011; *Qu et al*., 2011]. Considered together, these lines of evidence argue for the existence of an early Neoproterozoic (at least circa 0.9 Ga) ocean to the north of the Tarim Craton. Given the circa 0.9 Ga date for the oceanic crust and circa 750–700 Ma date for HP metamorphism, the oceanic crust was at least circa 150 Ma old when it was subducted, comparable with the oldest subducting ocean floor in the present West Pacific. Assuming continuous seafloor spreading with a rate of 2 cm/yr, a circa 3000 km wide ocean could have existed in the mid-Neoproterozoic. Therefore, the northern margin of the Tarim Craton could not have been a Grenvillian interior orogen that helped to weld together the Rodinia supercontinent. Any early Neoproterozoic tectonothermal events therein cannot be directly related to the assembly of Rodinia. Instead, the Tarim Craton may have been located at the periphery of Rodinia, with the northern margin facing the broad, long-lived, Panthalassa-type, Pan-Rodinia Ocean (also called Peri-Rodinia Ocean or Mirovoi Ocean), as adopted by *Li et al*. [2013] in the updated Rodinia reconstruction. This configuration allows for a protracted oceanic subduction and the development of an accretionary orogen in northern Tarim.

Recently *He et al*. [2012] reported circa 820–790 Ma granulites and mica schists of sedimentary affinities in the northernmost part of the Kuruktag area (Figure 1c). The relatively high pressure (circa 10 kbar) of peak metamorphism indicated burial of the supracrustal rocks to lower crustal levels. *Ge et al*. [2013a] also described a circa 830 Ma upper amphibolite to HP granulite facies metamorphic overprint of the Paleoproterozoic metasedimentary rocks and crustal anatexis in the Korla area. These regional metamorphic events can hardly be reconciled with a plume model but are consistent with a mid-Neoproterozoic accretionary orogen in northern Tarim.

The extensive circa 830–785 Ma granitoids in the Kuruktag area discussed above can also be better explained in terms of continental arc magmatism. These granitoids were mainly generated by relatively low-temperature, fluid-present partial melting of Archean mafic lower crust. As such ancient lower crust is essentially dry, especially after an earlier reworking as indicated by circa 1.9–1.8 Ga regional metamorphism and inherited metamorphic zircons, addition of a large amount of external fluids at a regional scale is necessary for crustal anatexis to generate the voluminous and widespread granitoids. Such a large-scale fluid addition is likely to occur in a subduction-related setting through direct slab dehydration or release from underplated hydrous mafic magmas. The circa 810 Ma Qigaibulake mafic-ultramafic-carbonatite complex in central Kuruktag is rich in volatiles, as indicated by abundant volatile-bearing phases in these rocks (e.g., phlogopite, apatite, and calcite) [*Zhang et al*., 2007; *Ye et al*., 2013]. These rocks may represent cumulates of such hydrous mantle melts, which were likely produced by relatively low-temperature, wet melting of the lithospheric mantle or mantle wedge, triggered by addition of fluids, rather than plume-related heating. An arc-related setting for these hydrous mantle rocks is consistent with the negative Nb-Ta-Ti, and locally also Zr-Hf, anomalies.

Furthermore, the increase of maximum Ho/Yb ratios (also La/Yb and Sr/Y ratios, figures not shown) of granitoids from 835 to 785 Ma in the Kuruktag area (Figure 12a) is consistent with rapid crustal thickening due to Andean-type subduction and advancing accretion. A compressional stress regime during this period is also supported by the regional high-grade metamorphism, weak foliation of some granitoids and sedimentary hiatus. Importantly, there is a sharp decrease in the maximum Ho/Yb ratios and increase in the average zircon saturation temperatures of the Kuruktag granitoids at circa 740 Ma (Figure 12b). This is coupled with a significant input of mantle-derived juvenile component to the magma source of the granitoids (Figure 11), as recorded by the sharp increase of zircon initial $^{176}Hf/^{177}Hf$ and the appearance of positive $\varepsilon Hf(t)$ values in the circa 740 Ma A-type granite [*Lei et al*., 2013] and circa 736 Ma bimodal intrusive complex [*Zhang et al*., 2012a]. This is also coincident with the onset of volcanic eruption and clastic deposition of the Beiyisi Formation

[*Xu et al*., 2005, 2009; *Gao et al*., 2010; *Zhang et al*., 2013], and is broadly coeval with the time of HP metamorphism and exhumation of the Aksu blueschist. These observations are best explained by a tectonic switch from an early episode of compression and crustal thickening due to advancing-type accretion, to a later extension and crustal thinning due to retreating-type accretion, probably resulting from slab rollback and trench retreat.

A tectonic switch from compression to extension can also explain the occurrence of abundant mafic dike swarms in the Kuruktag area [*Deng et al*., 2008; *Zhang et al*., 2009a, 2009b]. Geochemical and isotopic data indicate these mafic dykes were derived from subcontinental lithospheric mantle metasomatized by subduction-related fluids/melts, and they have been dated at circa 820 Ma and 780–770 Ma [*Deng et al*., 2008; *Zhang et al*., 2009a, 2009b]. However, it should be noted that most of these are based on zircon U-Pb ages and only one baddeleyite age of 773 ± 3 Ma has been reported [*Zhang et al*., 2009a]. As they intrude with sharp contacts into the granitoids as young as circa 785 Ma [*Long et al*., 2011a], the older zircon ages (circa 820 Ma) can best be interpreted as indicating a xenocryst origin. *Long et al*. [2011a] noted that a 754 ± 3 Ma quartz diorite in the same area was not intruded by these dikes. These observations suggest that the tectonic switch from compression to extension may have been initiated as early as circa 780 Ma, and that it took about 40 Ma for the transformation of the continental arc into an intra- or back-arc rift basin, within which the Beiyisi volcanic and clastic rocks were deposited.

The circa 660–630 Ma quartz syenite and syenogranite mostly record high zircon saturation temperatures (Figure 12b) and variable zircon Hf isotopic composition (Figure 11), suggesting high-temperature melting and magma mixing. The highly variable LILE and LREE contents of the quartz syenite suggest that the magma source and resultant melts were variously enriched in volatiles and fluid-mobile elements. The associated mafic dikes are also enriched in these mobile elements, probably including volatiles, as indicated by abundant hornblende and biotite in the spessartite dykes [*Zhu et al*., 2008, 2011b]. These dykes are variously depleted in Nb-Ta-Ti, and locally in Zr-Hf, which indicate an origin from lithospheric mantle metasomatized by subduction-related fluids [*Zhu et al*., 2011b]. The critical role of fluids in the petrogenesis of these rocks implies that subduction may have continued at least to circa 630 Ma and remained close to the northern margin of Tarim. Therefore, these rocks are better interpreted as having formed during continuous back-arc rifting, probably resulting from northward slab rollback and trench retreat. The abundant circa 615 Ma volcanic rocks in the Zhamoketi Formation in the Kuruktag area and circa 615–600 Ma basalts in the Aksu area [*Xu et al*., 2009, 2013; *He et al*., 2014] suggest that rifting continued for much longer.

4.3. Paleozoic Northern Margin of Tarim: Passive or Active?

As mentioned above, whether the northern margin of the Tarim Craton was an active or passive continental margin during the Paleozoic is a critical issue for understanding the subduction polarity of the paleo-oceanic plates within the Tianshan orogens and for the evolution of the southwestern CAOB. *Ge et al*. [2012a] first reported circa 420 Ma arc-related granitoids intruding the early Precambrian basement of the Tarim Craton in the Korla area. This was substantiated by further studies by *Guo et al*. [2013a, 2013b] and *Jia et al*. [2013] and data presented in this study. These data define an approximately 100 km long WNW-ESE trending magmatic belt dominated by calc-alkaline intermediate rocks and high-K calc-alkaline felsic rocks with intrusion ages ranging from 460 to 400 Ma (peak at circa 420 Ma) at the northern edge of the western Kuruktag area. These rocks intruded the Precambrian basement of the Tarim Craton and tectonic emplacement can be ruled out. As discussed above, the felsic rocks were partly derived from fluid-present melting in thickened lower crust, accompanied by the addition of juvenile mafic magma, whereas the more mafic rocks were generated by hydrous melting of mantle wedge and were variously contaminated by crustal material. Such a spatial-temporal distribution and petrogenetic scenario is consistent with an Andean-type continental arc setting for these rocks. Arc-related granitoids and volcanic rocks were also reported in the Huolashan [*Lin et al*., 2013] and Baicheng [*Huang et al*., 2013a] areas to the west and the Xinger [*Zhang and Sun*, 2010], Luobupo [*Xiao et al*., 2006], and Dunhuang [*Zhang et al*., 2009c] areas to the east, suggesting that such a continental arc was not restricted to the western Kuruktag but probably extended along the entire northern margin of the Tarim Craton.

The identification of a circa 460–400 Ma Andean-type continental arc indicates that, if the northern margin of the Tarim Craton was passive during the Cambrian to Middle Ordovician, it must have switched to an active margin as early as the Late Ordovician. Evidence for this tectonic switch is provided by an angular unconformity between Cambrian to Middle Ordovician carbonates and overlying Silurian to Devonian clastic rocks. *Ge et al*. [2012a] inferred that a retroarc foreland basin was created in the northern Tarim Basin.

This model is supported by recent tectono-stratigraphic analysis and detrital zircon provenance of Silurian to Devonian sandstones, which contain abundant circa 460–410 Ma euhedral magmatic zircons and were considered to be derived from a continental arc to the north [*Liu et al*., 2012].

The establishment of a Paleozoic northern Tarim continental arc generally supports the southward subduction model. However, according to previous authors, back-arc rifting and opening of the South Tianshan Ocean (STO) occurred during the Late Ordovician to Early Devonian, and southward subduction of the STO did not commence until circa 390 Ma [*Charvet et al*., 2007, 2011; *Lin et al*., 2009, 2013; *Wang et al*., 2010, 2011; *Ma et al*., 2014]. As pointed out previously, there is no evidence for such Paleozoic back-arc rifting on the Tarim side. Although most ophiolite mélanges within the South Tianshan were dated between circa 425 and 390 Ma [*Wang et al*., 2011; *Han et al*., 2011; and references therein], several older ophiolite mélanges have been documented recently. For example, *Yang et al*. [2011] reported SHRIMP zircon U-Pb ages of 439 ± 2 Ma for plagiogranite and 435 ± 3 Ma for anorthosite from the Yushugou ophiolite; *Zhang and Guo* [2008] reported a SHRIMP zircon U-Pb age of 516 ± 7 Ma for cumulate gabbro from the Hongliuhe ophiolite; *Ao et al*. [2012] reported a secondary ion mass spectrometry zircon U-Pb age of 533 ± 2 Ma for plagiogranite from the Yueyashan-Xichangjing ophiolite; and *Yang et al*. [2005] reported single zircon thermal ionization mass spectrometry ages of 590 ± 11 Ma and 600 ± 15 Ma for gabbro and basalt, respectively, from the Dalubayi ophiolite. Generally, the oldest ophiolite provides a minimum age for the opening of an oceanic basin. Accordingly, it can be inferred that the STO must have opened before Paleozoic. The suprasubduction zone geochemical feature, i.e., enrichment in LREE and LILE and depletion in HFSE, for the 533 ± 2 Ma Yueyashan-Xichangjing ophiolite [*Ao et al*., 2012] and the 392 ± 5 Ma Heiyingshan ophiolite [*Wang et al*., 2011] are consistent with a back-arc origin of the STO. However, the long evolutionary history (at least circa 200 Ma from 600 to 390 Ma) recorded by multiple ophiolites with different ages suggests that it may have developed into a complicated back-arc spreading system composed of multiple basins of different ages. The documentation of circa 460–400 Ma continental arc magmatism in northern Tarim suggests that southward subduction of this composite back-arc basin was initiated as early as Late Ordovician, about 70 Ma earlier than previously thought.

4.4. New Tectonic Model and its Implications

Traditionally, the Neoproterozoic and Paleozoic tectonothermal events were considered as two separated orogenic cycles. However, as discussed above, the northern Tarim margin probably faced a broad ocean with southward subduction throughout the mid-Neoproterozoic. Back-arc rifting and lithospheric extension due to northward slab rollback and trench retreat lasted until circa 615–600 Ma. This is broadly coeval with the oldest Dalubayi ophiolite mélange (circa 600–590 Ma) in the South Tianshan [*Yang et al*., 2005]. This allows us to link the Neoproterozoic accretionary orogenic system with the Paleozoic one and to propose a long-lived accretionary orogenic model (Figure 13).

In this model the greater Tarim Craton, including several microcontinent blocks within the Tianshan and Beishan orogens (e.g., the Yili, Central Tianshan, and Hanshan blocks) and at the southeastern margin (e.g., the Qaidam, Quanji, Qilian, and Alxa blocks), amalgamated along its southern margin to the northern periphery of the Rodinia supercontinent, probably with northwest Australia [*Li et al*., 2013]. The recent documentation of a circa 950–900 Ma (collisional?) orogenic belt in the Altyn Tagh-Qilian-Quanji-Qaidam areas [*Song et al*., 2012; *Yu et al*., 2013; *Wang et al*., 2013] provides a good candidate for such a suture zone. During or after amalgamation, subduction and accretion were initiated at the northern margin of the Tarim Craton, possibly as part of the circum-Rodinia subduction zone, in order to accommodate continuous seafloor spreading in the Pan-Rodinia Ocean [*Murphy and Nance*, 1991; *Cawood*, 2005; *Cawood and Buchan*, 2007]. As noted before, early Neoproterozoic (circa 950–900 Ma) arc-related magmatic rocks are abundant in the Yili, Central Tianshan, and Hanshan blocks to the north [*Chen et al*., 2009; *Hu et al*., 2010; *Peng et al*., 2012; *Huang et al*., 2013b]. However, geochronological data suggested that Neoproterozoic magmatism was insignificant until circa 830–780 Ma in northern Tarim, although abundant circa 900–830 Ma detrital zircons [e.g., *Zhu et al*., 2011a; *He et al*., 2014] hint that it may have initiated earlier. Recent studies showed that syn-orogenic metamorphism and crustal anatexis also occurred between circa 830 and 790 Ma [*He et al*., 2012; *Ge et al*., 2013a], rather than in the earliest Neoproterozoic, as previously thought [e.g., *Zhang et al*., 2012a]. Such southward younging of subduction-related tectonothermal events from the Tianshan to northern Tarim is consistent with a southward advancing accretionary orogen. The resultant compression, crustal thickening, and partial melting of different protoliths at different crustal depths can explain the selective deformation, high-grade metamorphism, regional unconformity, and diverse granitoid magmatism.

(A) ca. 950 - 780 Ma advancing type subduction-accretion (snapshot at ca. 830 Ma) as part of the Cirum-Rodinia subduction-accretion system

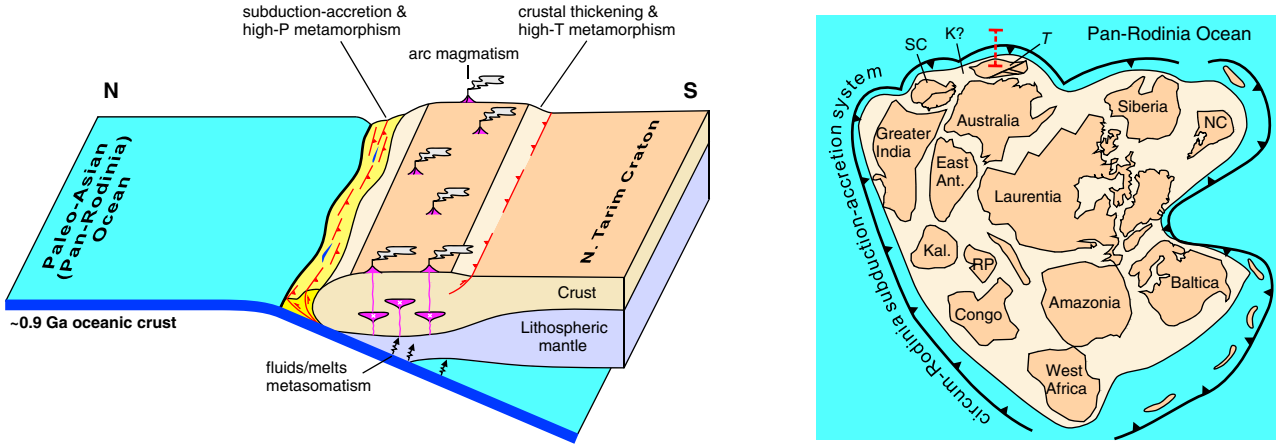

(B) ca. 780 - 600 Ma retreating type subduction-accretion (snapshot at ca. 600 Ma) leading to back-arc opening of the South Tianshan Ocean

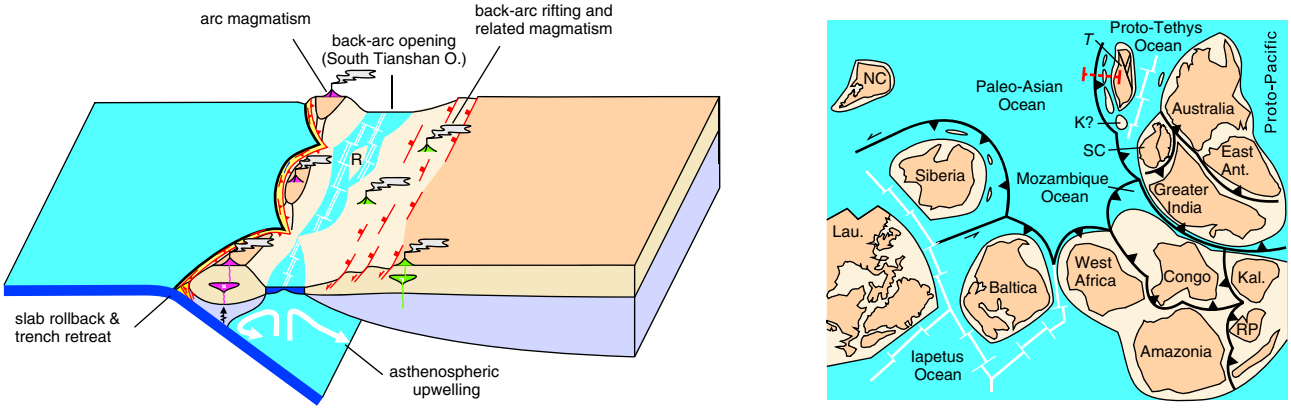

(C) ca. 460 - 400 Ma bi-directional subduction of the South Tianshan Ocean (snapshot at ca. 420 Ma) leading to amalgamation of Tarim and Kazakhstan

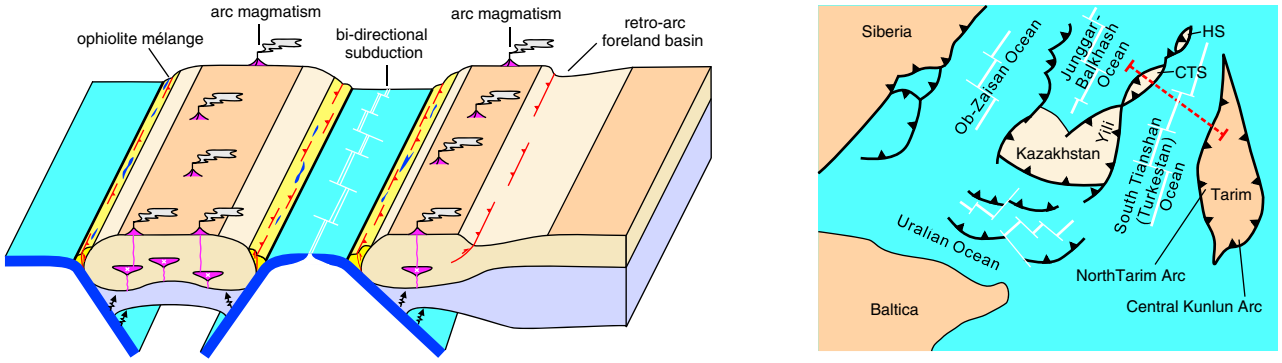

Figure 13. Geodynamic model and paleogeographical reconstruction for long-lived accretionary orogenesis in the northern Tarim Craton. (a) The circa 950–780 Ma advancing (Andean) type accretionary orogen initiated as part of the circum-Rodinia subduction-accretion system, resulting in southward migration of arc magmatism from the Tianshan (circa 950–900 Ma) to northern Tarim (circa 830–780 Ma). Rodinia reconstruction is modified after *Cawood et al.* [2013]. Position and orientation of Siberia and Tarim are according to *Hoffman* [1991] and *Li et al.* [2013], respectively. Ant. = Antarctica, K. = Kazakhstan, Kal. = Kalahari, NC = North China, RP = Rio de la Plata, SC = South China, T = Tarim. (b) The circa 780–600 Ma retreating (West Pacific) type accretionary orogen resulted in continuous back-arc rifting and, eventually, opening of the South Tianshan Ocean as a composite back-arc basin at circa 600 Ma. Note that the curved nature of the subduction zone resulted in separation of several discrete arc blocks (e.g., Yili, Central Tianshan, and Hanshan) and continental ribbons (R). Paleogeographical reconstruction is revised according to *Li et al.* [2013] and shows the opposite side of the globe relative to the map of *Li et al.* [2013]. The dimension of the oceans is not proportional. Laurentia (Lau.) is only partly shown. (c) Circa 460–400 Ma bidirectional subduction of the South Tianshan Ocean led to the amalgamation of Tarim with Kazakhstan and other parts of the CAOB. Only one arc is shown for simplicity, but the model may be applicable to arcs in the Yili, Central Tianshan (CTS), and Hanshan (HS) blocks. Paleogeographical reconstruction is modified after *Windley et al.* [2007].

An important tectonic switch from compression to extension occurred between circa 780 and 740 Ma and transformed the early advancing accretionary orogen into a retreating one. This is recorded by the intrusion of mafic dikes [*Zhang et al*., 2009a, 2009b], bimodal intrusive complexes [*Zhang et al*., 2012a] and A-type granites [*Lei et al*., 2013]. A back-arc rift basin was established at circa 740 on the southern (Kuruktag) part of the previous broad continental arc (Figure 13b) as indicated by the onset of volcanism and clastic sedimentation in the Beiyisi Formation [*Xu et al*., 2005, 2009; *Gao et al*., 2010; *Zhang et al*., 2013; *He et al*., 2014]. This is interpreted to be the result of large-scale northward slab rollback and trench retreat. Such a dynamic process also facilitated the exhumation of the Aksu blueschist [e.g., *Husson et al*., 2009]. Continuous back-arc rifting and lithospheric extension lasted to 660–630 Ma, as evidenced by the Korla mafic dyke-quartz syenite-syenogranite association [*Zhu et al*., 2008, 2011b; *Ge et al*., 2012b; this study]. Further rifting between circa 615 and 600 Ma is recorded by thick volcanic rocks in the Zhamoketi Formation in Kuruktag [*Xu et al*., 2009; *He et al*., 2014] and by the Sugetbrak Formation in the Aksu area [*Xu et al*., 2013], which eventually led to the detachment of the northern part of the early active margin as separate blocks (e.g., Yili, Central Tianshan, and Hanshan) and the opening of the South Tianshan Ocean. *Gao et al*. [1993] noted a widespread unconformity ("Liuquan Movement") underlying the Hankalchough diamictite (equivalent to the circa 582 Ma Gaskiers glacial deposits [*Xu et al*., 2009]) in the Kuruktag area as well as equivalent strata in the Yili, Central Tianshan, and Hanshan blocks, which is interpreted here as the breakup unconformity corresponding to the detachment of these blocks from Tarim. This process was probably followed by the separation of Tarim from northwest Australia with the opening of the Proto-Tethys Ocean, as constrained by the circa 524 Ma Kudi ophiolite in the West Kunlun area [*Zhang et al*., 2004] and circa 521 Ma Akesai ophiolite in the northern Altyn Tagh area [*Zhang et al*., 2009d]. During the Cambrian, the main southward subduction zone may have migrated to an oceanic domain in the Junggar region, as recorded by development of intraoceanic arcs as early as 510 Ma [e.g., *Ren et al*., 2014].

The South Tianshan Ocean may have initiated as a back-arc basin and later developed into a complicated back-arc spreading system composed of multiple basins of different ages (circa 600–390 Ma), separated by relict continental ribbons, analogous to the present back-arc basins in the Southwest Pacific (e.g., Tasman Sea) [*Schellart et al*., 2006]. The subduction of this composite back-arc basin may have commenced as early as the Late Ordovician, probably beneath both the Tarim Craton and the Yili-Central Tianshan-Hanshan Blocks, as recorded by circa 460–400 Ma continental arc magmatism documented above and in the Yili [e.g., *Gao et al*., 2009], Central Tianshan [e.g., *Ma et al*., 2014], and Hanshan [e.g., *Song et al*., 2013] blocks, respectively. Such a bidirectional subduction model [*Ge et al*., 2012a] is also consistent with the occurrence of two subparallel ophiolite belts to the north and south of the northern Tarim arc and the Yili-Central Tianshan-Hanshan arcs, respectively [*Han et al*., 2011]. This composite oceanic basin eventually closed by arc-continental collision during the Late Carboniferous, as recorded by HP-UHP metamorphic rocks and post-orogenic magmatism [*Han et al*., 2011, and references therein], although an alternative interpretation of Permian closure exists [e.g., *Xiao et al*., 2013].

The above model (Figure 13) highlights a long-lived (circa 950–300 Ma) and complicated accretionary orogenic history in the southwestern CAOB. It provides an interpretation for the origin of the microcontinental blocks (e.g., Yili, Central Tianshan, and Hanshan) of Tarim affinity within the southwestern CAOB. These blocks were the leading edge of this long-lived accretionary system; thus, they occupy a critical position to test this model. Continuous detrital zircon age spectra since the Neoproterozoic from the Central Tianshan Block [*Ma et al*., 2011, 2012] likely record magmatism within this long-lived arc, although the rock record is far from complete.

A good analogue to this long-lived accretionary orogenic model for the southwestern CAOB may be the Australian segment of the Terra Australis Orogen (i.e., the Tasmanides) [*Cawood*, 2005; *Glen*, 2013]. Here subduction of the Proto-Pacific Ocean toward the eastern Australia continental margin was initiated at circa 530 Ma as part of the marginal accretionary system of the Gondwana supercontinent immediately following its amalgamation and continues until the present day as manifested by active subduction in the SW Pacific [*Cawood*, 2005; *Cawood and Buchan*, 2007; *Glen*, 2013]. Thousands of kilometers of eastward or northeastward slab rollback and trench retreat since the Late Cretaceous resulted in episodic back-arc rifting, with sequential opening of several back-arc basins (e.g., the Tasman Sea, the New Caledonia, and South Fiji basins) and detachment of several continental blocks (e.g., Lord Howe Rise) [*Schellart et al*., 2006, and references therein]. Large-scale eastward trench retreat and back-arc extension probably also dominated the Terra Australis Orogen during the Paleozoic [e.g., *Cawood*, 2005; *Cawood and Buchan*, 2007; *Glen*, 2013], resulting in thick turbidites and voluminous granites in the back-arc basins, including the classic Lachlan I- and S-type granites [*Chappell and White*, 2001]. Such large-scale trench retreat and back-arc extension is a key to understanding the proposed long-lived

accretionary orogen of the southwestern CAOB, where the extended margins of northern Tarim and the rifted continental blocks in the Tianshan that were left inboard of Cambrian to Ordovician active subduction were long regarded as passive margins. One notable difference between the accretionary orogen in eastern Australian and that proposed for the southwestern CAOB is the lack of an early advancing accretionary phase in the former, although *Glen* [2013] suggested a short-lived phase of plate advance from 530 to 520 Ma. Another difference is the absence of episodic deformation of back-arc sequences for the southwestern CAOB (i.e., the Neoproterozoic to Ordovician rocks in northern Tarim). However, such episodic back-arc deformation was suggested to have resulted from the arrival and subduction of buoyant oceanic plateaus [*Collins*, 2002a, 2002b] and is thus serendipitous and is not an inevitable consequence of retreating-type subduction-accretion. Supporting this argument are the widespread late Mesozoic-Cenozoic back-arc basins in eastern China inboard of the West Pacific subduction zone, where thick rifting-subsidence sequences were never strongly deformed except for local structural inversion [e.g., *Ren et al*., 2002; *Ge et al*., 2012c].

Our model extends the accretionary orogenic history in the southwestern CAOB from the Paleozoic back into the early Neoproterozoic and links it with the circum-Rodinia accretionary system. This challenges many of the traditional models concerning the evolution of the CAOB, in which northern Tarim has been interpreted as a long-lived passive margin throughout the Neoproterozoic and Paleozoic [e.g., *Khain et al*., 2003; *Windley et al*., 2007]. It has been proposed that Siberia was located at the northern periphery of Rodinia adjacent to Laurentia, although the detailed position and orientation is debated [*Pisarevsky and Natapov*, 2003, and references therein]. It has also been well documented that the oldest ophiolite mélange and subduction-related magmatism along southern Siberia occurred as early as circa 1.0 Ga and progressively became younger to the south [*Windley et al*., 2007; *Kröner et al*., 2014; and references therein]. Therefore, it is reasonable to deduce that the southern margin of Siberia faced the Pan-Rodinia Ocean [*Hoffman*, 1991] and that subduction and accretion was also initiated as part of the circum-Rodinia accretionary system, comparable with that proposed for the northern Tarim. This also implies that the Paleo-Asian Ocean "intervening" between Siberia and Tarim is not a new-born ocean, but just a part of the Pan-Rodinia Ocean, and that accretion of the CAOB was not asymmetrical as previously thought [e.g., *Sengör et al*., 1993; *Windley et al*., 2007] but more like what is occurring in the present eastern and western Pacific, respectively.

5. Conclusions

1. Three episodes of granitoid intrusion occurred in the western Kuruktag area of the northern Tarim Craton: mid-Neoproterozoic (circa 830–820 Ma), late Neoproterozoic (circa 660–630 Ma), and Paleozoic (circa 420–400 Ma). The mid-Neoproterozoic granitoids were mainly generated by low-temperature, fluid-present partial melting of Archean mafic lower crust. The late Neoproterozoic and Paleozoic granitoids were probably both formed by magma mixing between juvenile and ancient crustal material, although from different sources at different melting temperatures and depths.
2. These granitoids, along with other petrological, geochronological, and isotopic data from the northern Tarim Craton, can be explained by a long-lived (950–300 Ma) accretionary orogenic model. This model involves an early phase of southward advancing-type accretion from the microcontinental blocks (at 950–900 Ma) in Tianshan to northern Tarim (at 830–780 Ma), and a later phase of retreating-type accretion due to northward slab rollback and trench retreat that led to back-arc rifting (at 780–600 Ma) and opening of the South Tianshan Ocean. The bidirectional subduction of the South Tianshan Ocean (circa 460–400 Ma) produced two subparallel magmatic arcs, namely the Yili-Central Tianshan-Hanshan arcs to the north and the northern Tarim arc to the south.
3. Our model extends the accretionary history in the southwestern CAOB from the Paleozoic back into the early Neoproterozoic and links it with the circum-Rodinia accretionary system, highlighting the symmetric accretionary systems relative to Tarim and Siberia.

Acknowledgments

We appreciate Z.X. Li and X.L. Wang for helpful discussions during this study, and M.Q. Zhang, B. Wu, and J.H. Yang for kind assistance during the geochemical, zircon U-Pb and Hf isotopic analyses, respectively. P.A. Cawood and an anonymous reviewer provided detailed reviews, which greatly improve this manuscript. This research was financially supported by grants from the Natural Science Foundation of China (41272211) and the State Key Laboratory for Mineral Deposits Research of Nanjing University (ZZKT-201110).

References

Andersen, T. (2002), Correction of common lead in U-Pb analyses that do not report ^{204}Pb, *Chem. Geol.*, *192*, 59–79, doi:10.1016/S0009-2541(02)00195-X.

Ao, S. J., W. J. Xiao, C. M. Han, X. H. Li, J. F. Qu, J. E. Zhang, Q. Q. Guo, and Z. H. Tian (2012), Cambrian to Early Silurian ophiolite and accretionary processes in the Beishan collage, NW China: Implications for the architecture of the Southern Altaids, *Geol. Mag.*, *149*, 606–625, doi:10.1017/S0016756811000884.

Cao, X. F., X. B. Lue, S. T. Liu, P. Zhang, X. Gao, C. Chen, and Y. L. Mo (2011), LA-ICP-MS zircon dating, geochemistry, petrogenesis and tectonic implications of the Dapingliang Neoproterozoic granites at Kuluketage Block, NW China, *Precambrian Res.*, *186*, 205–219, doi:10.1016/j.precamres.2011.01.017.

Cawood, P. A. (2005), Terra Australis Orogen: Rodinia breakup and development of the Pacific and Iapetus margins of Gondwana during the Neoproterozoic and Paleozoic, *Earth Sci. Rev.*, *69*, 249–279, doi:10.1016/j.earscirev.2004.09.001.

Cawood, P. A., and C. Buchan (2007), Linking accretionary orogenesis with supercontinent assembly, *Earth Sci. Rev.*, *82*, 217–256, doi:10.1016/j.earscirev.2007.03.003.

Cawood, P. A., A. Kröner, W. J. Collins, T. M. Kusky, W. D. Mooney, and B. F. Windley (2009), Accretionary orogens through Earth history, *Geol. Soc. London Spec. Publ.*, *318*(1), 1–36, doi:10.1144/SP318.1.

Cawood, P. A., Y. J. Wang, Y. J. Xu, and G. C. Zhao (2013), Locating South China in Rodinia and Gondwana: A fragment of greater India lithosphere?, *Geology*, doi:10.1130/G34395.1.

Chappell, B. W., and A. White (2001), Two contrasting granite types: 25 years later, *Aust. J. Earth Sci.*, *48*, 489–499, doi:10.1046/j.1440-0952.2001.00882.x.

Charvet, J., L. S. Shu, and S. Laurent-Charvet (2007), Paleozoic structural and geodynamic evolution of eastern Tianshan (NW China): Welding of the Tarim and Junggar Plates, *Episodes*, *30*, 162–186.

Charvet, J., L. S. Shu, S. Laurent-Charvet, B. Wang, M. Faure, D. Cluzel, Y. Chen, and K. De Jong (2011), Paleozoic tectonic evolution of the Tianshan Belt, NW China, *Sci. China Earth Sci.*, *54*, 166–184, doi:10.1007/s11430-010-4138-1.

Chen, Y., B. Xu, S. Zhan, and Y. G. Li (2004), First mid-Neoproterozoic Paleomagnetic results from the Tarim Basin (NW China) and their geodynamic implications, *Precambrian Res.*, *133*, 271–281, doi:10.1016/j.precamres.2004.05.002.

Chen, X. Y., Y. J. Wang, L. H. Sun, and W. M. Fan (2009), Zircon SHRIMP U-Pb dating of the granitic gneisses from Bingdaban and Laerdundaban (Tianshan Orogen) and their geological significances, *Geochemica*, *38*, 424–431.

Collins, W. J. (2002a), Hot orogens, tectonic switching, and creation of continental crust, *Geology*, *30*, 535–538, doi:10.1130/0091-7613(2002)030<0535:HOTSAC>2.0.CO;2.

Collins, W. J. (2002b), Nature of extensional accretionary orogens, *Tectonics*, *21*(4), 1024, doi:10.1029/2000TC001272.

Collins, W. J., E. A. Belousova, A. Kemp, and J. B. Murphy (2011), Two contrasting Phanerozoic orogenic systems revealed by hafnium isotope data, *Nat. Geosci.*, *4*, 333–337, doi:10.1038/ngeo1127.

Cox, K. G., J. D. Bell, and R. J. Pankhurst (1979), *The Interpretation of Igneous Rocks*, George Allen and Unwin, London.

Defant, M. J., and M. S. Drummond (1990), Derivation of some modern arc magmas by melting of young subducted lithosphere, *Nature*, *347*, 662–665, doi:10.1038/347662a0.

Deng, X. L., L. S. Shu, W. B. Zhu, D. S. Ma, and B. Wang (2008), Precambrian tectonism, magmatism, deformation and geochronology of igneous rocks in the Xingdi Fault Zone, Xinjiang, *Acta Petrol. Sin.*, *24*, 2800–2808.

Frost, B. R., C. G. Barnes, W. J. Collins, R. J. Arculus, D. J. Ellis, and C. D. Frost (2001), A geochemical classification for granitic rocks, *J. Petrol.*, *42*, 2033–2048, doi:10.1093/petrology/42.11.2033.

Gao, Z. J., J. B. Chen, S. N. Lu, C. W. Peng, and Z. Y. Qin (1993), The Precambrian geology in northern Xinjiang (Precambrian geology no. 6), Geological Publishing House, Beijing.

Gao, J., L. L. Long, R. Klemd, Q. Qian, D. Y. Liu, X. M. Xiong, W. Su, W. Liu, Y. T. Wang, and F. Q. Yang (2009), Tectonic evolution of the South Tianshan orogen and adjacent regions, NW China: Geochemical and age constraints of granitoid rocks, *Int. J. Earth Sci.*, *98*, 1221–1238, doi:10.1007/s00531-008-0370-8.

Gao, L. Z., Z. Q. Wang, Z. Q. Xu, J. S. Yang, and W. Zhang (2010), A new evidence from zircon SHRIMP U-Pb dating of the Neoproterozoic diamictite in Quruqtagh area, Tarim Basin, Xinjiang, China, *Geol. Bull. China*, *29*, 205–213.

Gao, J., R. Klemd, Q. Qian, X. Zhang, J. L. Li, T. Jiang, and Y. Q. Yang (2011), The collision between the Yili and Tarim Blocks of the southwestern Altaids: Geochemical and age constraints of a leucogranite dike crosscutting the HP-LT metamorphic belt in the Chinese Tianshan Orogen, *Tectonophysics*, *499*, 118–131, doi:10.1016/j.tecto.2011.01.001.

Ge, R. F., W. B. Zhu, H. L. Wu, B. H. Zheng, X. Q. Zhu, and J. W. He (2012a), The Paleozoic northern margin of the Tarim Craton: Passive or active?, *Lithos*, *142–143*, 1–15, doi:10.1016/j.lithos.2012.02.010.

Ge, R. F., W. B. Zhu, B. H. Zheng, H. L. Wu, J. W. He, and X. Q. Zhu (2012b), Early Pan-African magmatism in the Tarim Craton: Insights from zircon U–Pb–Lu–Hf isotope and geochemistry of granitoids in the Korla area, NW China, *Precambrian Res.*, *212–213*, 117–138, doi:10.1016/j.precamres.2012.05.001.

Ge, R. F., Q. L. Zhang, L. S. Wang, J. Chen, G. A. Xie, and X. Y. Wang (2012c), Late Mesozoic rift evolution and crustal extension in the central Songliao Basin, northeastern China: Constraints from cross-section restoration and implications for lithospheric thinning, *Int. Geol. Rev.*, *54*, 183–207, doi:10.1080/00206814.2010.511900.

Ge, R. F., W. B. Zhu, H. L. Wu, B. H. Zheng, and J. W. He (2013a), Timing and mechanisms of multiple episodes of migmatization in the Korla Complex, northern Tarim Craton, NW China: Constraints from zircon U–Pb–Lu–Hf isotopes and implications for crustal growth, *Precambrian Res.*, *231*, 136–156, doi:10.1016/j.precamres.2013.03.005.

Ge, R. F., W. B. Zhu, H. L. Wu, J. W. He, and B. H. Zheng (2013b), Zircon U–Pb ages and Lu–Hf isotopes of Paleoproterozoic metasedimentary rocks in the Korla Complex, NW China: Implications for metamorphic zircon formation and geological evolution of the Tarim Craton, *Precambrian Res.*, *231*, 1–18, doi:10.1016/j.precamres.2013.03.003.

Glen, R. A. (2013), Refining accretionary orogen models for the Tasmanides of eastern Australia, *Aust. J. Earth Sci.*, *60*, 315–370, doi:10.1080/08120099.2013.772537.

Guo, R. Q., A. Nijiati, Q. Qin, X. L. Jia, Z. X. Zhu, K. Z. Wang, and Y. P. Li (2013a), Geological characteristics and tectonic significance of Silurian granitic intrusions in the northern Tarim craton, Xinjiang, *Geol. Bull. China*, *32*, 220–238.

Guo, R. Q., Q. Qin, Z. Muhetaer, L. L. Zhao, M. J. Sui, and Z. Wei (2013b), Geological characteristics and tectonic significance of Ordovician granite intrusions in the western segment of Quruqtagh, Xinjiang, *Earth Sci. Front.*, *20*, 255–267.

Han, B. F., G. Q. He, X. C. Wang, and Z. J. Guo (2011), Late Carboniferous collision between the Tarim and Kazakhstan–Yili terranes in the western segment of the South Tian Shan Orogen, Central Asia, and implications for the Northern Xinjiang, western China, *Earth Sci. Rev.*, *109*, 74–93, doi:10.1016/j.earscirev.2011.09.001.

Hanchar, J. M., and E. B. Watson (2003), Zircon saturation thermometry, *Rev. Mineral. Geochem.*, *53*, 89–112, doi:10.2113/0530089.

He, Z. Y., Z. M. Zhang, K. Q. Zong, W. Wang, and M. Santosh (2012), Neoproterozoic granulites from the northeastern margin of the Tarim Craton: Petrology, zircon U-Pb ages and implications for the Rodinia assembly, *Precambrian Res.*, *212-213*, 21–33, doi:10.1016/j.precamres.2012.04.014.

He, J. W., W. B. Zhu, and R. F. Ge (2014), New age constraints on Neoproterozoic diamicites in Kuruktag, NW China and Precambrian crustal evolution of the Tarim Craton, *Precambrian Res.*, *241*, 44–60, doi:10.1016/j.precamres.2013.11.005.

Hoffman, P. F. (1991), Did the breakout of Laurentia turn Gondwanaland inside-out?, *Science*, *252*, 1409–1412, doi:10.1126/science.252.5011.1409.
Hu, A. Q., G. J. Wei, B. M. Jiang, J. B. Zhang, W. F. Deng, and L. L. Chen (2010), Formation of the 0.9 Ga Neoproterozoic granitoids in the Tianshan Orogen, NW China: Constraints from the SHRIMP zircon age determination and its tectonic significance, *Geochimica*, *39*, 197–212.
Huang, B. T., Z. Y. He, K. Q. Zong, and Z. M. Zhang (2013a), Zircon U–Pb and Hf isotopic study of Neoproterozoic granitic gneisses from the Alatage area, Xinjiang: Constraints on the Precambrian crustal evolution in the Central Tianshan Block, *China Sci. Bull.*, *59*, 100–112, doi:10.1007/s11434-013-0010-y.
Huang, H., Z. C. Zhang, M. Santosh, D. Y. Zhang, Z. D. Zhao, and J. L. Liu (2013b), Early Paleozoic tectonic evolution of the South Tianshan collisional belt: Evidence from geochemistry and zircon U-Pb geochronology of the Tie'reke monzonite pluton, northwest China, *J. Geol.*, *121*, 401–424, doi:10.1086/670653.
Husson, L., J. Brun, P. Yamato, and C. Faccenna (2009), Episodic slab rollback fosters exhumation of HP–UHP rocks, *Geophys. J. Int.*, *179*, 1292–1300, doi:10.1111/j.1365-246X.2009.04372.x.
Jia, X. L., R. Q. Guo, F. M. Chai, A. Nijiati, Q. Qin, Z. X. Zhu, and K. Z. Wang (2013), Geochemistry and geochronology of monzogranites in Kuruktag of Xinjiang and their tectonic implications, *Geol. Bull. China*, *23*, 239–250.
Khain, E. V., E. V. Bibikova, E. B. Salnikova, A. Kroner, A. S. Gibsher, A. N. Didenko, K. E. Degtyarev, and A. A. Fedotova (2003), The Palaeo-Asian ocean in the Neoproterozoic and early Palaeozoic: New geochronologic data and palaeotectonic reconstructions, *Precambrian Res.*, *122*, 329–358, doi:10.1016/S0301-9268(02)00218-8.
Kröner, A., et al. (2014), Reassessment of continental growth during the accretionary history of the Central Asian Orogenic Belt, *Gondwana Res.*, *25*, 103–125, doi:10.1016/j.gr.2012.12.023.
Lei, R. X., C. Z. Wu, G. X. Chi, G. Chen, L. X. Gu, and Y. H. Jiang (2012), Petrogenesis of the Paleoproterozoic Xishankou pluton, northern Tarim block, northwest China: Implications for assembly of the supercontinent Columbia, *Int. Geol. Rev.*, *54*, 1829–1842, doi:10.1080/00206814.2012.678045.
Lei, R. X., C. Z. Wu, G. X. Chi, L. X. Gu, L. H. Dong, X. Qu, Y. H. Jiang, and S. Y. Jiang (2013), The Neoproterozoic Hongliujing A-type granite in Central Tianshan (NW China): LA-ICP-MS zircon U-Pb geochronology, geochemistry, Nd-Hf isotope and tectonic significance, *J. Asian Earth Sci.*, *74*, 142–154, doi:10.1016/j.jseaes.2013.03.025.
Li, Z. X., and S. J. Zhong (2009), Supercontinent-superplume coupling, true polar wander and plume mobility: Plate dominance in whole-mantle tectonics, *Phys. Earth Planet. Inter.*, *176*, 143–156, doi:10.1016/j.pepi.2009.05.004.
Li, Z. X., L. Zhang, and C. M. Powell (1996), Positions of the East Asian cratons in the Neoproterozoic supercontinent Rodinia, *Aust. J. Earth Sci.*, *43*, 593–604, doi:10.1080/08120099608728281.
Li, Z. X., X. H. Li, P. D. Kinny, and J. Wang (1999), The breakup of Rodinia: Did it start with a mantle plume beneath South China?, *Earth Planet. Sci. Lett.*, *173*, 171–181, doi:10.1016/S0012-821X(99)00240-X.
Li, Z. X., et al. (2008), Assembly, configuration, and break-up history of Rodinia: A synthesis, *Precambrian Res.*, *160*, 179–210, doi:10.1016/j.precamres.2007.04.021.
Li, Z. X., D. A. Evans, and G. Halverson (2013), Neoproterozoic glaciations in a revised global palaeogeography from the breakup of Rodinia to the assembly of Gondwanaland, *Sediment. Geol.*, *294*, 219–232, doi:10.1016/j.sedgeo.2013.05.016.
Lin, W., M. Faure, Y. H. Shi, Q. C. Wang, and Z. Li (2009), Palaeozoic tectonics of the south-western Chinese Tianshan: New insights from a structural study of the high-pressure/low-temperature metamorphic belt, *Int. J. Earth Sci.*, *98*, 1259–1274, doi:10.1007/s00531-008-0371-7.
Lin, W., Y. Chu, W. B. Ji, Z. P. Zhang, Y. H. Shi, Z. Y. Wang, Z. Li, and Q. C. Wang (2013), Geochronological and geochemical constraints for a middle Paleozoic continental arc on the northern margin of the Tarim block: Implications for the Paleozoic tectonic evolution of the South Chinese Tianshan, *Lithosphere*, *5*, 355–381, doi:10.1130/L231.1.
Liou, J. G., et al. (1989), Proterozoic blueschist belt in western China: Best documented Precambrian blueschists in the world, *Geology*, *17*, 1127–1131, doi:10.1130/0091-7613(1989)017<1127:PBBIWC>2.3.CO;2.
Liou, J. G., S. A. Graham, S. Maruyama, and R. Y. Zhang (1996), Characteristics and tectonic significance of the Late Proterozoic Aksu blueschists and diabasic dikes, northwest Xinjiang, China, *Int. Geol. Rev.*, *38*, 228–244, doi:10.1080/00206819709465332.
Lister, G., and M. Forster (2009), Tectonic mode switches and the nature of orogenesis, *Lithos*, *113*, 274–291, doi:10.1016/j.lithos.2008.10.024.
Liu, X. C., B. L. Chen, B. M. Jahn, G. G. Wu, and Y. S. Liu (2011), Early Paleozoic (circa 465 Ma) eclogites from Beishan (NW China) and their bearing on the tectonic evolution of the southern Central Asian Orogenic Belt, *J. Asian Earth Sci.*, *42*, 715–731, doi:10.1016/j.jseaes.2010.10.017.
Liu, J. Y., H. J. Yang, Y. H. Yang, Z. Z. Cai, Y. Q. Liu, Z. F. Rui, and Z. Z. Su (2012), The U-Pb chronologic evidence and sedimentary responses of Silurian tectonic activities at northeastern margin of Tarim Basin, *Sci. China Ser. D Earth Sci.*, *55*, 1445–1460, doi:10.1007/s11430-012-4466-4.
Long, X. P., C. Yuan, M. Sun, G. C. Zhao, W. J. Xiao, Y. J. Wang, Y. H. Yang, and A. Q. Hu (2010), Archean crustal evolution of the northern Tarim Craton, NW China: Zircon U-Pb and Hf isotopic constraints, *Precambrian Res.*, *180*, 272–284, doi:10.1016/j.precamres.2010.05.001.
Long, X. P., C. Yuan, M. Sun, A. Kröner, G. C. Zhao, S. Wilde, and A. Q. Hu (2011a), Reworking of the Tarim Craton by underplating of mantle plume-derived magmas: Evidence from Neoproterozoic granitoids in the Kuluketage area, NW China, *Precambrian Res.*, *187*, 1–14, doi:10.1016/j.precamres.2011.02.001.
Long, X. P., C. Yuan, M. Sun, W. J. Xiao, G. C. Zhao, K. F. Zhou, Y. J. Wang, and A. Q. Hu (2011b), The discovery of the oldest rocks in the Kuluketage area and its geological implications, *Sci. China Ser. D Earth Sci.*, *54*, 342–348, doi:10.1007/s11430-010-4156-z.
Lu, S. N., H. K. Li, C. L. Zhang, and G. H. Niu (2008), Geological and geochronological evidence for the Precambrian evolution of the Tarim Craton and surrounding continental fragments, *Precambrian Res.*, *160*, 94–107, doi:10.1016/j.precamres.2007.04.025.
Ma, X. X., L. S. Shu, B. M. Jahn, W. B. Zhu, and M. Faure (2011), Precambrian tectonic evolution of Central Tianshan, NW China: Constraints from U–Pb dating and in situ Hf isotopic analysis of detrital zircons, *Precambrian Res.*, *222–223*, 450–473, doi:10.1016/j.precamres.2011.06.004.
Ma, X. X., L. S. Shu, M. Santosh, and J. Y. Li (2012), Detrital zircon U–Pb geochronology and Hf isotope data from Central Tianshan suggesting a link with the Tarim Block: Implications on Proterozoic supercontinent history, *Precambrian Res.*, *206–207*, 1–16, doi:10.1016/j.precamres.2012.02.015.
Ma, X. X., L. S. Shu, J. G. Meert, and J. Y. Li (2014), The Paleozoic evolution of Central Tianshan: Geochemical and geochronological evidence, *Gondwana Res.*, *25*, 797–819, doi:10.1016/j.gr.2013.05.015.
Martin, H., R. H. Smithies, R. Rapp, J. F. Moyen, and D. Champion (2005), An overview of adakite, tonalite-trondhjemite-granodiorite (TTG), and sanukitoid: Relationships and some implications for crustal evolution, *Lithos*, *79*, 1–24, doi:10.1016/j.lithos.2004.04.048.
Miller, C. F., S. M. McDowell, and R. W. Mapes (2003), Hot and cold granites? Implications of zircon saturation temperatures and preservation of inheritance, *Geology*, *31*, 529–532, doi:10.1130/0091-7613(2003)031<0529:HACGIO>2.0.CO;2.
Murphy, J. B., and R. D. Nance (1991), Supercontinent model for the contrasting character of Late Proterozoic orogenic belts, *Geology*, *19*, 469–472, doi:10.1130/0091-7613(1991)019<0469:SMFTCC>2.3.CO;2.
Nakajima, T., S. Maruyama, S. Uchiumi, J. G. Liou, X. Wang, X. Xiao, and S. A. Graham (1990), Evidence for late Proterozoic subduction from 700-Myr-old blueschists in China, *Nature*, *346*, 263–265, doi:10.1038/346263a0.
O'Connor, J. T. (1965), A classification for Quartz-rich igneous rocks based on feldspar ratios, in *Geological Survey Professional Paper*, vol. 525, pp. 79–84, USGS, Colorado, Denver.

Patiño Douce, A. E. (1997), Generation of metaluminous A-type granites by low-pressure melting of calc-alkaline granitoids, *Geology*, *25*, 743–746, doi:10.1130/0091-7613(1997)025<0743:GOMATG>2.3.CO;2.
Patiño Douce, A. E., and J. S. Beard (1995), Dehydration-melting of biotite gneiss and quartz amphibolite from 3 to 15 kbar, *J. Petrol.*, *36*, 707–738, doi:10.1093/petrology/36.3.707.
Peccerillo, A., and S. R. Taylor (1976), Geochemistry of Eocene calc-alkaline volcanic rocks from the Kastamonu area, Northern Turkey, *Contrib. Mineral. Petrol.*, *58*, 63–81, doi:10.1007/BF00384745.
Peng, X. M., C. G. Zhong, Q. H. Zuo, W. M. Zhu, S. W. Yang, and X. Huang (2012), The formation age and their geological significance of gneissose granites neighbouring Kawabulake area in East Tianshan Mountain, *Xingjiang Geol.*, *30*, 12–18.
Pisarevsky, S. A., and L. M. Natapov (2003), Siberia and Rodinia, *Tectonophysics*, *375*, 221–245, doi:10.1016/j.tecto.2003.06.001.
Qian, Q., and J. Hermann (2013), Partial melting of lower crust at 10–15 kbar: Constraints on adakite and TTG formation, *Contrib. Mineral. Petrol.*, *165*, 1195–1224, doi:10.1007/s00410-013-0854-9.
Qu, J. F., W. J. Xiao, B. F. Windley, C. M. Han, Q. G. Mao, S. J. Ao, and J. E. Zhang (2011), Ordovician eclogites from the Chinese Beishan: Implications for the tectonic evolution of the southern Altaids, *J. Metamorph. Geol.*, *29*, 803–820, doi:10.1111/j.1525-1314.2011.00942.x.
Rapp, R. P., E. B. Watson, M. P. Roberts, and J. D. Clemens (1995), Dehydration melting of metabasalt at 8–32 kbar—Implications for continental growth and crust-mantle recycling; origin of high-potassium, calc-alkaline, I-type granitoids, *J. Petrol.*, *36*, 891–931, doi:10.1093/petrology/36.4.891.
Ren, J. Y., K. Tamaki, S. T. Li, and J. X. Zhang (2002), Late Mesozoic and Cenozoic rifting and its dynamic setting in eastern China and adjacent areas, *Tectonophysics*, *344*, 175–205, doi:10.1016/S0040-1951(01)00271-2.
Ren, R., et al. (2014), When did the subduction first initiate in the southern Paleo-Asian Ocean: New constraints from a Cambrian intra-oceanic arc system in West Junggar, NW China, *Earth Planet. Sci. Lett.*, *388*, 222–236, doi:10.1016/j.epsl.2013.11.055.
Schellart, W. P. (2008), Overriding plate shortening and extension above subduction zones: A parametric study to explain formation of the Andes Mountains, *Geol. Soc. Am. Bull.*, *120*, 1441–1454, doi:10.1130/B26360.1.
Schellart, W. P., G. S. Lister, and V. G. Toy (2006), A Late Cretaceous and Cenozoic reconstruction of the Southwest Pacific region: Tectonics controlled by subduction and slab rollback processes, *Earth Sci. Rev.*, *76*, 191–233, doi:10.1016/j.earscirev.2006.01.002.
Schmidt, M. W., and S. Poli (2004), Magmatic epidote, *Rev. Mineral. Geochem.*, *56*, 399–430, doi:10.2138/gsrmg.56.1.399.
Sen, C., and T. Dunn (1994), Dehydration melting of a basaltic composition amphibolite at 1.5 and 2.0 Gpa—Implications for the origin of adakites, *Contrib. Mineral. Petrol.*, *117*, 394–409, doi:10.1007/BF00307273.
Sengör, A. M. C., B. A. Natal'In, and V. S. Burtman (1993), Evolution of the Altaid tectonic collage and Palaeozoic crustal growth in Eurasia, *Nature*, *364*, 299–307, doi:10.1038/364299a0.
Shand, S. J. (1943), *Eruptive Rocks*, John Wiley, New York.
Shu, L. S., X. L. Deng, W. B. Zhu, D. S. Ma, and W. J. Xiao (2011), Precambrian tectonic evolution of the Tarim Block, NW China: New geochronological insights from the Quruqtagh domain, *J. Asian Earth Sci.*, *42*, 774–790, doi:10.1016/j.jseaes.2010.08.018.
Singh, J., and W. Johannes (1996), Dehydration melting of tonalites. Part II. Composition of melts and solids, *Contrib. Mineral. Petrol.*, *125*, 26–44, doi:10.1007/s004100050204.
Song, S. G., L. Su, X. H. Li, Y. L. Niu, and L. F. Zhang (2012), Grenville-age orogenesis in the Qaidam-Qilian block: The link between South China and Tarim, *Precambrian Res.*, *220–221*, 9–22, doi:10.1016/j.precamres.2012.07.007.
Song, D. F., W. J. Xiao, C. M. Han, J. L. Li, J. F. Qu, Q. Q. Guo, L. N. Lin, and Z. M. Wang (2013), Progressive accretionary tectonics of the Beishan orogenic collage, southern Altaids: Insights from zircon U–Pb and Hf isotopic data of high-grade complexes, *Precambrian Res.*, *227*, 368–388, doi:10.1016/j.precamres.2012.06.011.
Sun, S. S., and W. F. McDonough (1989), Chemical and isotopic systematics of oceanic basalts: Implications for mantle composition and processes, *Geol. Soc. London Spec. Publ.*, *42*, 313–345, doi:10.1144/GSL.SP.1989.042.01.19.
Uyeda, S., and H. Kanamori (1979), Back-arc opening and the mode of subduction, *J. Geophys. Res.*, *84*, 1049–1061, doi:10.1029/JB084iB03p01049.
Wang, B., M. Faure, L. S. Shu, K. De Jong, J. Charvet, D. Cluzel, B. M. Jahn, Y. Chen, and G. Ruffet (2010), Structural and geochronological study of high pressure metamorphic rocks in the Kekesu Section (northwestern China): Implications for the Late Paleozoic tectonics of the southern Tianshan, *J. Geol.*, *118*, 59–77, doi:10.1086/648531.
Wang, B., L. S. Shu, M. Faure, B. M. Jahn, D. Cluzel, J. Charvet, S. L. Chung, and S. Meffre (2011), Paleozoic tectonics of the southern Chinese Tianshan: Insights from structural, chronological and geochemical studies of the Heiyingshan ophiolitic mélange (NW China), *Tectonophysics*, *497*, 85–104, doi:10.1016/j.tecto.2010.11.004.
Wang, C., L. Liu, W. Yang, X. Zhu, Y. Cao, L. Kang, S. Chen, R. Li, and S. He (2013), Provenance and ages of the Altyn Complex in Altyn Tagh: Implications for the early Neoproterozoic evolution of northwestern China, *Precambrian Res.*, *230*, 193–208, doi:10.1016/j.precamres.2013.02.003.
Watson, E. B., and T. M. Harrison (1983), Zircon saturation revisited—Temperature and composition effects in a variety of crustal magma types, *Earth Planet. Sci. Lett.*, *64*, 295–304, doi:10.1016/0012-821X(83)90211-X.
Wen, B., Y. X. Li, and W. B. Zhu (2013), Paleomagnetism of the Neoproterozoic diamictites of the Qiaoenbrak formation in the Aksu area, NW China: Constraints on the paleogeographic position of the Tarim Block, *Precambrian Res.*, *226*, 75–90, doi:10.1016/j.precamres.2012.10.018.
Whalen, J. B., K. L. Currie, and B. W. Chappell (1987), A-type granites—Geochemical characteristics, discrimination and petrogenesis, *Contrib. Mineral. Petrol.*, *95*, 407–419, doi:10.1007/BF00402202.
Wilhem, C., B. F. Windley, and G. M. Stampfli (2012), The Altaids of Central Asia: A tectonic and evolutionary innovative review, *Earth Sci. Rev.*, *113*, 303–341, doi:10.1016/j.earscirev.2012.04.001.
Windley, B. F., D. Alexeiev, W. J. Xiao, A. Kröner, and G. Badarch (2007), Tectonic models for accretion of the Central Asian Orogenic Belt, *J. Geol. Soc. London*, *164*, 31–47, doi:10.1144/0016-76492006-022.
Wolf, M. B., and P. J. Wyllie (1994), Dehydration-melting of amphibolite at 10 kbar: The effects of temperature and time, *Contrib. Mineral. Petrol.*, *115*, 369–383, doi:10.1007/BF00320972.
Xinjiang Bureau of Geology and Mineral Resources (XBGMR) (1993), *Regional Geology of Xinjiang Uygur Autonomy Region*, Geological Publishing House, Beijing.
Xiao, L., and J. D. Clemens (2007), Origin of potassic (C-type) adakite magmas: Experimental and field constraints, *Lithos*, *95*, 399–414, doi:10.1016/j.lithos.2006.09.002.
Xiao, P. X., Y. H. Huang, Y. X. Wang, and X. A. Wang (2006), Geochemical characteristics and isotope dating of moyite at the southeastern margin of the Kuruktag block, Xinjiang, China, *Geol. Bull. China*, *25*, 725–729.
Xiao, W. J., B. C. Huang, C. M. Han, S. Sun, and J. L. Li (2010), A review of the western part of the Altaids: A key to understanding the architecture of accretionary orogens, *Gondwana Res.*, *18*, 253–273, doi:10.1016/j.gr.2010.01.007.
Xiao, W. J., B. F. Windley, M. B. Allen, and C. M. Han (2013), Paleozoic multiple accretionary and collisional tectonics of the Chinese Tianshan orogenic collage, *Gondwana Res.*, *23*, 1316–1341, doi:10.1016/j.gr.2012.01.012.

Xu, B., P. Jian, H. F. Zheng, H. B. Zou, L. F. Zhang, and D. Y. Liu (2005), U-Pb zircon geochronology and geochemistry of Neoproterozoic volcanic rocks in the Tarim Block of northwest China: Implications for the breakup of Rodinia supercontinent and Neoproterozoic glaciations, *Precambrian Res.*, *136*, 107–123, doi:10.1016/j.precamres.2004.09.007.

Xu, B., S. H. Xiao, H. B. Zou, Y. Chen, Z. X. Li, B. Song, D. Y. Liu, C. M. Zhou, and X. L. Yuan (2009), SHRIMP zircon U-Pb age constraints on Neoproterozoic Quruqtagh diamictites in NW China, *Precambrian Res.*, *168*, 247–258, doi:10.1016/j.precamres.2008.10.008.

Xu, B., H. Zou, Y. Chen, J. He, and Y. Wang (2013), The Sugetbrak basalts from northwestern Tarim Block of northwest China: Geochronology, geochemistry and implications for Rodinia breakup and ice age in the Late Neoproterozoic, *Precambrian Res.*, *236*, 214–226, doi:10.1016/j.precamres.2013.07.009.

Yang, H. B., P. Gao, B. Li, and Q. J. Zhang (2005), The geological character of the Sinian Dalubayi ophiolite in the west Tianshan, Xinjiang, *Xinjiang Geol.*, *23*, 123–126.

Yang, J. S., C. L. Wu, S. Y. Chen, R. D. Shi, J. X. Zhang, F. C. Meng, G. C. Zuo, H. Q. Wu, and C. Elena (2006), Neoproterozoic eclogitic metamorphic age of the Beishan eclogite of Gansu, China: Evidence from SHRIMP U-Pb isotope dating, *Geol. China*, *33*, 317–325.

Yang, J. S., X. Z. Xu, T. F. Li, S. Y. Chen, Y. F. Ren, J. Y. Li, and Z. Liu (2011), U-Pb ages of zircons from ophiolite and related rocks in the Kumishi region at the southern margin of Middle Tianshan, Xinjiang: Evidence of Early Paleozoic oceanic basin, *Acta Petrol. Sin.*, *27*, 77–95.

Ye, H. M., X. H. Li, and Z. W. Lan (2013), Geochemical and Sr-Nd-Hf-O-C isotopic constraints on the origin of the Neoproterozoic Qieganbulake ultramafic-carbonatite Complex from the Tarim Block, Northwest China, *Lithos*, *182–183*, 150–164, doi:10.1016/j.lithos.2013.10.002.

Yong, W. J., L. F. Zhang, C. M. Hall, S. B. Mukasa, and E. J. Essene (2012), The $^{40}Ar/^{39}Ar$ and Rb-Sr chronology of the Precambrian Aksu blueschists in western China, *J. Asian Earth Sci.*, *63*, 197–205, doi:10.1016/j.jseaes.2012.05.024.

Yu, S. Y., J. X. Zhang, P. G. Del Real, X. L. Zhao, K. J. Hou, J. H. Gong, and Y. S. Li (2013), The Grenvillian orogeny in the Altun–Qilian–North Qaidam mountain belts of northern Tibet Plateau: Constraints from geochemical and zircon U–Pb age and Hf isotopic study of magmatic rocks, *J. Asian Earth Sci.*, *73*, 372–395, doi:10.1016/j.jseaes.2013.04.042.

Zhan, S., Y. Chen, B. Xu, B. Wang, and M. Faure (2007), Late Neoproterozoic paleomagnetic results from the Sugetbrak Formation of the Aksu area, Tarim basin (NW China) and their implications to paleogeographic reconstructions and the snowball Earth hypothesis, *Precambrian Res.*, *154*, 143–158, doi:10.1016/j.precamres.2007.01.001.

Zhang, Y. Y., and Z. J. Guo (2008), Accurate constraint on formation and emplacement age of Hongliuhe ophiolite, boundary region between Xinjiang and Gansu Provinces and its tectonic implications, *Acta Petrol. Sin.*, *24*, 803–809.

Zhang, Y., and X. M. Sun (2010), $^{40}Ar/^{39}Ar$ dating on the Late Devonian volcanic rocks from Kuruktag and its implications for regional geology, Xinjiang, *Acta Petrol. Sin.*, *26*, 302–308.

Zhang, C. L., H. F. Yu, J. L. Shen, Y. G. Dong, H. M. Ye, and K. Y. Guo (2004), Zircon SHRIMP age determination of the giant-crystal gabbro and basalt in Kuda, West Kunlun: Dismembering of the Kuda Ophiolite, *Geol. Rev.*, *50*, 639–643.

Zhang, C. L., Z. X. Li, X. H. Li, H. M. Ye, A. G. Wang, and K. Y. Guo (2006), Neoproterozoic bimodal intrusive complex in the southwestern Tarim Block, northwest China: Age, geochemistry, and implications for the rifting of Rodinia, *Int. Geol. Rev.*, *48*, 112–128, doi:10.2747/0020-6814.48.2.112.

Zhang, C. L., X. H. Li, Z. X. Li, S. N. Lu, H. M. Ye, and H. M. Li (2007), Neoproterozoic ultramafic-mafic-carbonatite complex and granitoids in Quruqtagh of northeastern Tarim Block, western China: Geochronology, geochemistry and tectonic implications, *Precambrian Res.*, *152*, 149–169, doi:10.1016/j.precamres.2006.11.003.

Zhang, C. L., Z. X. Li, X. H. Li, and H. M. Ye (2009a), Neoproterozoic mafic dyke swarms at the northern margin of the Tarim Block, NW China: Age, geochemistry, petrogenesis and tectonic implications, *J. Asian Earth Sci.*, *35*, 167–179, doi:10.1016/j.jseaes.2009.02.003.

Zhang, Z. C., Z. J. Guo, G. Q. Zou, Z. S. Feng, and H. F. Li (2009b), Geochemical characteristics and SHRIMP U-Pb age of zircons from the Danghe reservoir TTG in Dunhuang, Gansu Province, and its significations, *Acta Petrol. Sin.*, *25*, 495–505.

Zhang, Z. C., Z. J. Guo, and B. Song (2009c), SHRIMP zircon dating of gabbro from the ophiolite melange in the northern Altyn Tagh and its geological implications, *Acta Petrol. Sin.*, *25*, 568–576.

Zhang, Z. Y., W. B. Zhu, L. S. Shu, J. B. Su, and B. H. Zheng (2009d), Neoproterozoic ages of the Kuluketage diabase dyke swarm in Tarim, NW China, and its relationship to the breakup of Rodinia, *Geol. Mag.*, *146*, 150–154, doi:10.1017/S0016756808005839.

Zhang, C. L., H. B. Zou, H. Y. Wang, H. K. Li, and H. M. Ye (2012a), Multiple phases of the Neoproterozoic igneous activity in Quruqtagh of the northeastern Tarim Block, NW China: Interaction between plate subduction and mantle plume?, *Precambrian Res.*, *222–223*, 488–502, doi:10.1016/j.precamres.2011.08.005.

Zhang, C. L., H. K. Li, M. Santosh, Z. X. Li, H. B. Zou, H. Y. Wang, and H. M. Ye (2012b), Precambrian evolution and cratonization of the Tarim Block, NW China: Petrology, geochemistry, Nd-isotopes and U–Pb zircon geochronology from Archaean gabbro-TTG–potassic granite suite and Paleoproterozoic metamorphic belt, *J. Asian Earth Sci.*, *47*, 5–20, doi:10.1016/j.jseaes.2011.05.018.

Zhang, Y. L., Z. Q. Wang, Z. Yan, and T. Wang (2013), Neoproterozoic volcanic rocks in the southern Quruqtagh of Northwest China: Geochemistry, zircon geochronology and tectonic implications, *Acta Geol. Sin. Engl. Ed.*, *87*, 118–130.

Zhao, P., Y. Chen, S. Zhan, B. Xu, and M. Faure (2014), The Apparent Polar Wander Path of the Tarim block (NW China) since the Neoproterozoic and its implications for a long-term Tarim–Australia connection, *Precambrian Res.*, *242*, 39–57, doi:10.1016/j.precamres.2013.12.009.

Zheng, B. H., W. B. Zhu, B. M. Jahn, L. S. Shu, Z. Y. Zhang, and J. B. Su (2010), Subducted Precambrian oceanic crust: Geochemical and Sr-Nd isotopic evidence from metabasalts of the Aksu blueschist, NW China, *J. Geol. Soc. London*, *167*, 1161–1170, doi:10.1144/0016-76492010-001.

Zhu, W. B., Z. Y. Zhang, L. S. Shu, H. F. Lu, J. B. Su, and W. Yang (2008), SHRIMP U-Pb zircon geochronology of Neoproterozoic Korla mafic dykes in the northern Tarim Block, NW China: Implications for the long-lasting breakup process of Rodinia, *J. Geol. Soc. London*, *165*, 887–890, doi:10.1144/0016-76492007-174.

Zhu, W. B., B. H. Zheng, L. S. Shu, D. S. Ma, H. L. Wu, Y. X. Li, W. T. Huang, and J. J. Yu (2011a), Neoproterozoic tectonic evolution of the Precambrian Aksu blueschist terrane, northwestern Tarim, China: Insights from LA-ICP-MS zircon U-Pb ages and geochemical data, *Precambrian Res.*, *185*, 215–230, doi:10.1016/j.precamres.2011.01.012.

Zhu, W. B., B. H. Zheng, L. S. Shu, D. S. Ma, J. L. Wan, D. W. Zheng, Z. Y. Zhang, and X. Q. Zhu (2011b), Geochemistry and SHRIMP U–Pb zircon geochronology of the Korla mafic dykes: Constrains on the Neoproterozoic continental breakup in the Tarim Block, northwest China, *J. Asian Earth Sci.*, *42*, 791–804, doi:10.1016/j.jseaes.2010.11.018.